Tool-Based Haptic Interaction with Dynamic Physical Simulations using Lorentz Magnetic Levitation

Peter Berkelman
Robotics Thesis Proposal

July 27, 1997

Abstract

I propose for my thesis project to build a high-performance 6 degree of freedom magnetic levitation haptic interface device, integrate its operation for use with realistic, detailed, graphically displayed three-dimensional simulated physical environments, and evaluate the effectiveness of the resulting rigid-body haptic interaction system.

In tool-based haptic interaction, the user feels and interacts with the simulated environment through a rigid tool of a given shape rather than directly with the hand and fingers. Consequently, a tool-based haptic interaction device only needs to control the dynamics of the rigid-body tool grasped by the user, rather than stimulate the user's skin, joints, or muscles directly. Tool-based human tasks such as cutting, pushing, screwing, probing, and inserting can all be simulated with tool-based haptic interaction.

An ideal haptic interface would enable simulated virtual objects to be sensed and manipulated in exactly the same natural and intuitive manner as real objects in the world. The high dexterity and sensitivity of the human hand provides a rich and direct medium for interaction between the user and the simulated world. Psychophysical studies have shown that the haptic sensitivity of the human hand extends to the micron level with a bandwidth of at least several hundred Hertz [1, 2]. To realistically emulate the experience of handling real objects, the haptic interface system must reproduce object dynamics at the same high level of detail and responsiveness. To achieve this performance requires a device with stiff and lightweight moving parts, powerful and responsive actuators, high resolution sensors, and a fast, low latency control system.

Lorentz levitation technology [3] is especially well suited to high-performance tool-based haptic interaction because it provides motion and force feedback in 6 DOF with very high control bandwidths and sensitivity, non-contact actuation and position sensing, and only one moving part. The magnetic levitation haptic interaction system under development provides a comfortable range of motion for the fingertips for fine haptic tasks and is totally enclosed in a desktop-height cabinet. A complete evaluation of the dynamic performance of the maglev device will be performed to demonstrate its potential for realistic haptic interaction.

I plan to integrate a physically-based realtime dynamic simulation of rigid objects and added surface effects of texture and friction with the haptic interface. An intermediate representation scheme for the local simulated environment will be developed and implemented to maintain consistency between the device controller and the physical simulation and to determine the correct rigid-body behavior of the haptic device between the much slower updates of the physical simulation. The effectiveness of the haptic interface system will be demonstrated by simulating the execution of sample haptic tasks.

Contents

List of Figures

1 Introduction

This research will explore the new issues in 6 degrees of freedom [DOF] haptic interaction which arise from the sensitivity and response bandwidths which can be realized using Lorentz magnetic levitation.

Haptic sensing refers to the sensing modalities of the hand, or more generally the sense of touch or feeling. The haptic sense is a combination of tactile sensing which is local sensation from nerve receptors in the skin, and kinesthetic sensing, which is due to internal distributed sensation in the joints and muscles. Comprehensive surveys of psychophysical, perceptual, sensitivity and bandwidth issues in human haptic sensing are given by Shimoga and Cholewiak and Collins in [1, 2].

Humans use dexterous motion of the hand together with the sense of touch and feel to gain information about the dynamics and surface characteristics of our environment when we grasp, squeeze, push, pick up, manipulate, or touch the surface of objects. The synthesis of haptic sensing with dexterous motion is *haptic exploration* or *haptic interaction*.

To enable haptic interaction with a virtual environment, a device is needed which can reproduce the haptically sensed characteristics of objects such as shape and stiffness and preferably more subtle characteristics such as surface friction and texture. The realism of the haptic interaction is determined by how well the speed, resolution, and sensitivity of the haptic interface device duplicates the characteristics of the simulated environment, up to the limits of human hand sensitivity.

The development and widespread availability of faster computer processing, cheaper memory, and improved algorithms make it possible to simulate more and more complex dynamic physical environments in real time with the modeling of collision and friction between multiple objects. A high-performance haptic interface device, fully integrated with a graphical display and a physical simulation as pictured in Fig. 1 could give its user convincing interaction with a realistic environment. Comprehensive surveys in the current state-of-the-art in haptic interfaces are given in [4] and [5].

The main potential applications of haptic interaction are in the areas of CAD, biomolecular analysis, medical simulation, and entertainment. A haptic interface to a CAD system would enable a user to directly feel subtleties of the fit, surface finish, and inertia of modelled parts. Haptic interaction with medical simulations would allow a surgeon in training to realistically feel and manipulate body tissues. An additional possible application is the haptic exploration of abstract, nonphysical space: A user could move in and feel any arbitrary properties representable in a vector field, such as fluid flow, pressure, magnetic field, or any potential field gradient.

1.1 Haptic Interaction Issues

The most important performance criteria for a haptic interaction device are its sensitivity, or position resolution, and its responsiveness, or control bandwidths. There is an important distinction to be made between force and position bandwidths: The force control bandwidth of a device determines the maximum frequency at which device can generate desired forces and the position bandwidth is the maximum frequency that the motion of the device can follow. For a force-actuated device with position feedback, the force bandwidth will be much greater since it depends only on the time constants of the actuators and any backlash in the transmissions or joints, but the position bandwidth is limited by the sensor bandwidths, the control rate and gains, and the inertia of the moving parts.

Performance tradeoffs and acceptable impedance bounds for free and constrained motion were established experimentally in [6]. Mechanical control issues of haptic interface devices such as impedance range, control bandwidth and stability have been examined by Colgate *et al.* [7]. One of the main conclusions of this study was the overwhelming benefit of passive damping in the device for stable control over a wide range of device impedance.

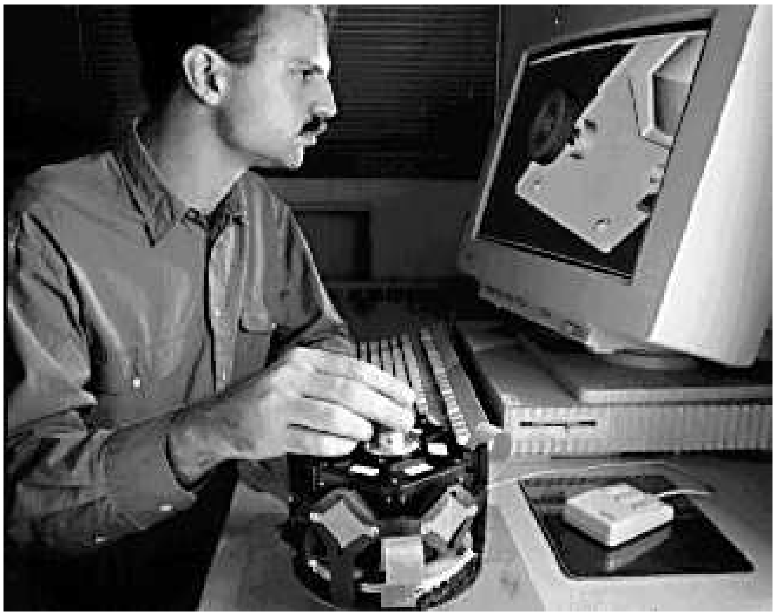

Figure 1: Using a Desktop Maglev Haptic Interface Device with a Graphical Display

Brooks' group at the University of North Carolina established Project GROPE for evaluation of spatial object placement and molecular docking tasks in virtual physical environments using 6 DOF haptic interfaces [8]. In their experiments, user performance was approximately doubled with the addition of force feedback. One of the observations from this research was that the manipulator arm haptic interfaces they were using were marginally adequate and noted that mechanical backlash, static friction, and other motion problems were "very troublesome". In their experience, a haptic device using finger and hand motions would be preferable to arm motions since the relative sensitivity of the hand and fingers is at least as great as the arm and hand, and finger-hand motions are less tiring.

With a 6 DOF device, the user can both locate and orient virtual objects with a single interaction in an intuitive, direct way which is not possible with any combination of lower dimensionality devices. In [9], Waters and Wang used 6 DOF input devices to manipulate objects and interact with a synthetic 3-D environment and concluded that the tasks considered would be very difficult with lower dimensionality devices.

A compact, inexpensive 6 DOF input device called Magellan or the Space Mouse has recently been widely commercialized by the German Aerospace Research Establishment and Logitech for robot control and 3-D CAD interaction[10]. The user guide reports that "flying an object in 6 DOF is done intuitively without any strain". It was found that users preferred to manipulate a small rounded puck shape with the fingertips than to grasp a large ball with the entire hand, since fingertip manipulation is more sensitive and less tiring.

Taken together, the conclusions of the task device interaction studies described above suggest that an ideal device would fulfill the following criteria:

- passive damping
- finger-hand motion
- negligible backlash and static friction

- 6 DOF of motion and force feedback

The maglev haptic interface device described in Part I meets all the above criteria. Its control bandwidths and impedance range will be maximized by minimizing the device inertia and maximizing the control rate.

1.2 Previous Haptic Interface Devices

Haptic interface devices can be classified according to whether they are body-referenced (fixed to the user) or ground-referenced (fixed to a stationary base), whether they provide tactile or force feedback, whether they enclose or are grasped by the user, whether they are operated by the entire arm, hand, or fingers only, and by how many degrees of freedom of motion or force they provide. The development of haptic interface devices began from large, heavy serial manipulators used as force-reflecting hand controller masters and has progressed to increasingly fast, lightweight, and sensitive exoskeleton, linkage, and tensioned cable devices. The main reported performance parameters of several existing force/kinesthesis based devices are summarized in Table 1.

Bergamasco and others [11] have developed force-reflecting exoskeleton systems; others are commercially available[12, 13]. Haptic exoskeletons may be either be supported by a fixed base or by the user's body only. Exoskeleton devices generally have the large inertia typical of serial linkage manipulators and fit may be a problem for users of different sizes.

Tensioned cable systems for haptic interaction have been developed at JPL, Tokyo Institute of Technology, and the University of Texas at Austin[14, 15, 16]. In these systems, a handle grasped by the user is supported from all directions by several actuated cables. The combined tension in the cables produces a net force and torque on the user's hand. The workspace of the device can be made very large while the actuated inertia remains small.

A lightweight 3 DOF linkage called the PHANToM [17] was developed at MIT and is commercially produced by SensAble Technologies, Inc. The user interacts with this device through a fingertip thimble or grasped stylus. An optional encoder gimbal adds 3 DOF of orientation sensing but no feedback forces. The Pantograph, [18] developed at McGill University, is a small 2 DOF planar linkage with low inertias and reported to be capable of high bandwidths.

A 6 DOF platform called the HapticMaster was developed by Iwata at the University of Tsukuba and is commercially produced by Nissho Electronics[19]. The moving platform of this device is supported by three 3 DOF pantograph linkages, resulting in redundant actuation with 9 DOF. A compact pen-based 7 DOF linkage and tendon device is under development at McGill University which aims to provide dynamic response to 50-100 Hz, forces from 1 mN to 10 N, and variation in mechanical impedance over 3 orders of magnitude [20].

Tactile haptic perception has been studied with various small devices attached on the hand which use vibration, heat, pin arrays, or pneumatic bladders to simulate tactile contact and pressure with virtual objects. Specialized force-reflecting devices have been made for simulations of specific medical procedures, such as laparoscopy [21], eye surgery [22], and other medical procedures [23].

The haptic interaction approach to be used here is Lorentz force magnetic levitation technology. The advantages of Lorentz magnetic levitation over conventional motors and linkages for haptic interaction device actuation are non-contact actuation, high force and motion control bandwidths, and 6 DOF in a compact device with only one moving part. This means of haptic interaction has previously been demonstrated with the IBM Magic Wrist [24] and the UBC wrist [25]. I propose to use a new maglev device, designed specifically for haptic interaction and with a larger range of motion and more

Device Type	DOF	Force Range	Motion Range	Bandwidth	Resolutions
Texas 9-string	6	43.4 N, 4.8 N-m	450 mm dia. sphere	$<$10 Hz pos.	NA
SPIDAR II	6-12	4 N/cable	300 mm dia. sphere	30 Hz force	0.5 mm
NWU Stewart Platform	4	45 N, 1.35 N-m	200x80 mm	$<$100 Hz	0.05^o
U. Tsukuba Pen	6	5 N	440 mm dia. sphere	$<$10 Hz pos.	2 mm
PER-Force	6	53 N	100 mm, 90-180^o	100 Hz	7.5 μm, 0.01^o
PHANToM	3	8.5 N	130x180x250 mm	800 Hz force	0.03 mm
HapticMaster	6	69 N, 0.5 N-m	400 mm dia. sphere	50 Hz force	0.4 mm
Magic Wrist & UBC Wrist	6	20N	$\pm$4.5 mm,$\pm 6^o$	15-50 Hz pos. 3000 Hz force	$< 5\mu$m
Proposed Device	6	60 N, 3 N-m	$>$ 25 mm sphere, $\pm 12^o$	$>$ 100 Hz pos.	3 μm

Data taken from [4] and others.

Table 1: Published Haptic Interface Device Parameters

comfortable form for manipulation, for high-performance haptic interaction with a physically-based simulated environment with added effects of friction and texture.

1.3 Outline

Part I of this proposal describes hardware and control aspects including the design, function, fabrication, proposed performance testing experiments, and results for the proposed haptic interface device. Section 2 reviews previous Lorentz maglev devices and their shortcomings for haptic interaction, followed by the motivation and goals for a new maglev device, then presents the overall configuration of the new device design. The actuation and sensing subsystems and the proposed control methods to be used are described in sections 3, 4, and 5. The fabrication methods used for the device and the current status of the control implementation are given next. The main expected contributions of the new maglev device, including the design, experimental evaluation, and use of the device as an interaction testbed, are given in the final section of Part I.

Part II describes the proposed integration of the interface device with physical simulations. Additional user interaction modes and the graphical display are described in section 9. Principles of realtime physically-based simulation are reviewed and previous and proposed work on emulating texture and friction effects for solid body contact are described in section 10. The proposed technique for integrating the physical simulation, surface friction and texture emulation, and the control of the maglev device for haptic interaction is described in section 11. The separation of the physical simulation and the device controller computations and the use of local intermediate representations to link the fast device controller and the slower physical simulations are are also described in that section. Proposed sample tasks to be modelled and simulated in order to evaluate the effectiveness of the haptic interaction system and the proposed user evaluation methods are described in section 12. The final section of Part II is a review of the expected contributions of the proposed research performed with the complete interaction system. The thesis proposal concludes with a proposed research plan schedule, acknowledgements, and references.

Part I
New Maglev Haptic Interface Device

2 Design

To stably levitate a free object in space, a maglev device must have at least six actuators to control the six DOF of the levitated object. A Lorentz force actuator consists of a fixed magnet assembly and a current-carrying wire coil. The areas of the coil that are in the magnetic field experience a generated force

$$\boldsymbol{f} = \oint \boldsymbol{B} \times \boldsymbol{I} d\boldsymbol{l}$$

where $\boldsymbol{l}$ is the length of the wire in the coil, $\boldsymbol{B}$ is the magnetic field, and $\boldsymbol{I}$ is the current in the wire. The actuation of the maglev device is analogous to a Stewart platform since all the actuators operate in parallel between a fixed base and a single moving platform. To provide position error feedback to the control system, non-contact position sensors are needed. In the following descriptions the levitated part of the device will be referred to as the *flotor* and the stationary base as the *stator*.

The new device described here is the first Lorentz maglev device that is specifically designed for haptic interaction. Previous research using magnetic levitation fine motion wrists demonstrated the feasibility of Lorentz magnetic levitation for haptic interaction, but also revealed the shortcomings of these positioning devices for haptics. The new design was completed by carefully evaluating desired characteristics for the device and finding a balance among conflicting requirements. The Pro/Engineer parametric solid modelling CAD package was used throughout the design process for visualization, ease of modifications, calculation of part clearances, and preparation of part drawings for fabrication.

2.1 Previous Lorentz Maglev Devices

The first Lorentz force magnetic levitation device was the *Magic Wrist* [24] developed at IBM T.J. Watson Research Center. This device was originally designed as a fine-motion robot wrist for coarse-fine manipulation and later adapted for use as a haptic interface for mechanism emulation, solid contacts, and texture and friction experiments [26]. The magnet assemblies in this device are arranged in inner and outer rings and the flotor coils are embedded in the sides of a hexagonal box. Three position sensing photodiodes on the inside of the flotor and three narrow-beam LEDs on the stator are used for position sensing. Its force, motion, and bandwidth parameters are also given in Table 1.

Due to the hexagonal shape of the flotor, the ranges of motion in translation and rotation are not independent. At the maximum translation, the rotation range decreases to zero, and similarly there is no translation range at the maximum rotation, because the edges and corners of the hexagonal box flotor collide with the magnet assemblies. These limitations of the Magic Wrist are not a problem when the wrist is carried by a 6 DOF robot arm, but as a haptic interface device it is difficult for the user to haptically recognize shape features scaled down to a motion range of under 10 mm.

The UBC Wrist[25] is another 6 DOF Lorentz force magnetic levitation device that has been used as a teleoperation master, as a fine motion wrist, and for haptic interaction [27]. The UBC wrist is smaller and has a more compact arrangement of actuators but it has a similar cylindrical shape. Its inertia is 0.65 kg and position and force control bandwidths and ranges of force and motion are similar to the Magic Wrist.

Both the IBM magic wrist and the UBC wrist were designed as compact fine motion robot wrists for high position accuracy and sensitivity, so their limited motion range and non-ergonomic shape was

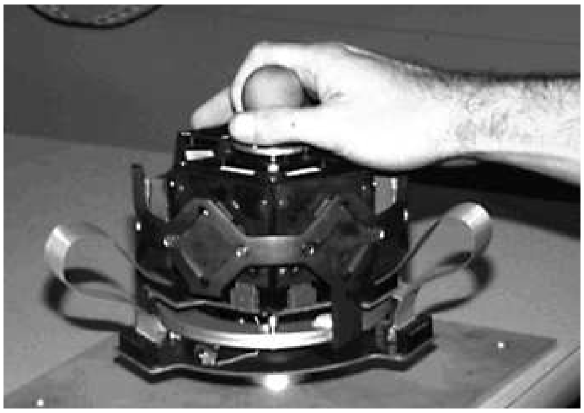

Figure 2: Magic Wrist

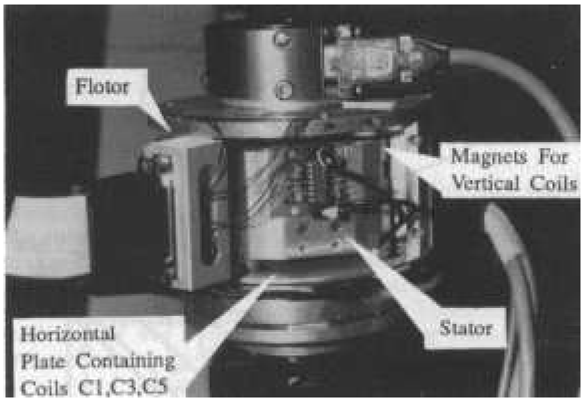

Figure 3: UBC Wrist

not a consideration.

2.2 Design Goals

The small, coupled ranges of translation and rotation in the Magic wrist and UBC wrist (<10 mm and <10°) severely limit the user's sensation of interaction and haptic shape perception in the simulated environment. The squat cylindrical shape of both devices makes them awkward to grasp and manipulate, which reduces the effectiveness of the haptic interaction. Ideally, the flotor should be grasped at the center of a rounded shape, so that the range of rotation is equal in all directions and nearly decoupled from translation. Although the control bandwidths of the maglev devices are an improvement over most linkage devices, the bandwidths could be increased by increasing the controller sample rate and reducing the inertia of the flotor. Furthermore, the complexity and number of parts in the completed device could be reduced.

To correct these shortcomings a new device was designed for haptic interaction. The new device aims to significantly increase the force and motion ranges and bandwidths and provide a more ergonomic handle for the user to manipulate while retaining the force and position sensitivity of the older devices. The expected performance parameters of the device are given in Table 1. A comfortable hand grip is located at the center of rotation of the flotor and the translation range will be at least 25 mm in all directions with as much rotation as possible to accommodate the typical fingertip motions for common tool handling tasks. Since the purpose of the device is fine haptic interaction using the fingertips, a motion range for arm motion is not necessary. The complete system including the device, amplifiers, power supplies, control processors, network communication, and analog I/O is contained in a single desktop-height cabinet enclosure so that it can be easily rolled up next to a desk and used with a graphical workstation.

2.3 New Configuration

The new device flotor is a hemispherical shell with a handle at its center. With this shape, the flotor can be rotated about its center without colliding with the stator. The ranges of rotation and translation are independent and equal in all directions. The user can reach in and grasp a handle located at its center. The flotor coils, the free space around the flotor, and the magnet assemblies in the stator or base must must all conform to the spherically curved shape. Additional details of the device design

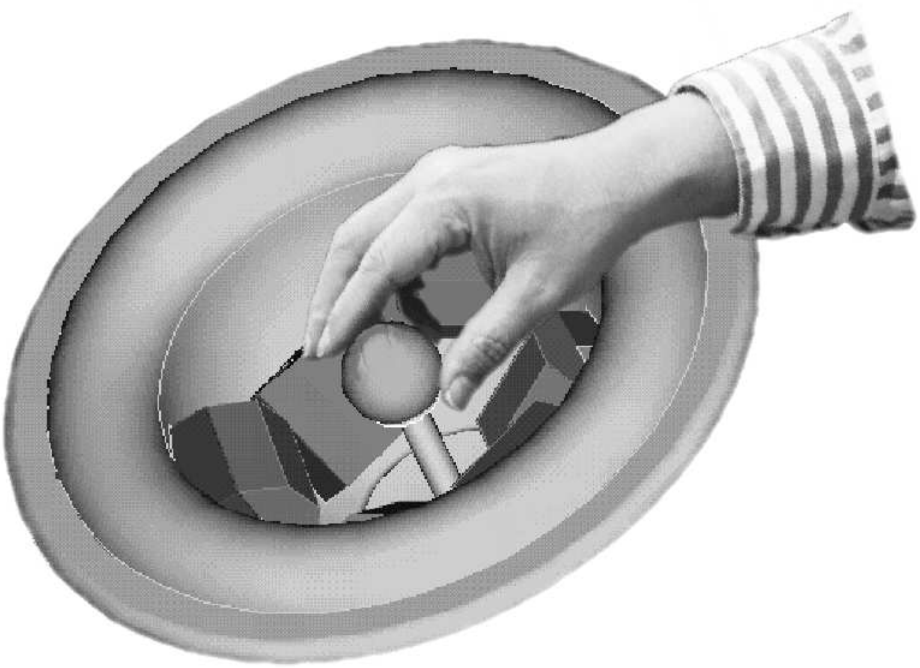

Figure 4: Hand Operation of the Haptic Device

are described in [28].

The entire device is embedded in a compact desk-height enclosure with the flotor handle and the top rim of the stator at the level of the desktop surface. This configuration allows the user's wrist and forearm to rest on the stator rim and desktop while the haptic device handle is manipulated with the fingertips. This position is more comfortable and less tiring for manipulation and results in more sensitive fingertip control for the user since the weight of the hand is supported by the stator. The position of the user's hand during operation of the haptic device is shown in Fig. 4.

To conform to the new hemispherical geometry and the increased range of motion, the actuator configuration, magnet assemblies, and the position sensing system was completely redesigned. Fig. 5 shows a cutaway representation of the device showing the principal parts including the levitated flotor, the stator enclosure, magnet and sensor assemblies, and the tool handle.

The flotor should have minimal levitated mass but high stiffness for the best performance. The main body of the flotor is a thin hemispherical aluminum shell with large oval cutouts for the actuator coils. The coils fit together in a densely packed configuration to maximize the area on the flotor used to generate actuation forces. LEDs for position sensing fit snugly between the coils. The coils are wound from ribbon wire on spherical forms to fit the curvature of the flotor. The design of the flotor assembly with the hemispherical shell, actuator coils, LEDs, and handle is shown in Fig. 6. Although the flotor mass is concentrated in the hemispherical shell, it is still easy to manipulate with one hand since the total mass is low and the weight is supported by actuation forces during use.

One drawback of Lorentz levitation actuation is that the range of motion of the device is limited by the width of the air gap in the magnetic assemblies. As a result, the 25-30 mm range of motion of this device is smaller than most other haptic interface devices. Since the aim of this device is to enable fine, dextrous, local haptic interaction using the fingertips rather than with large-scale arm

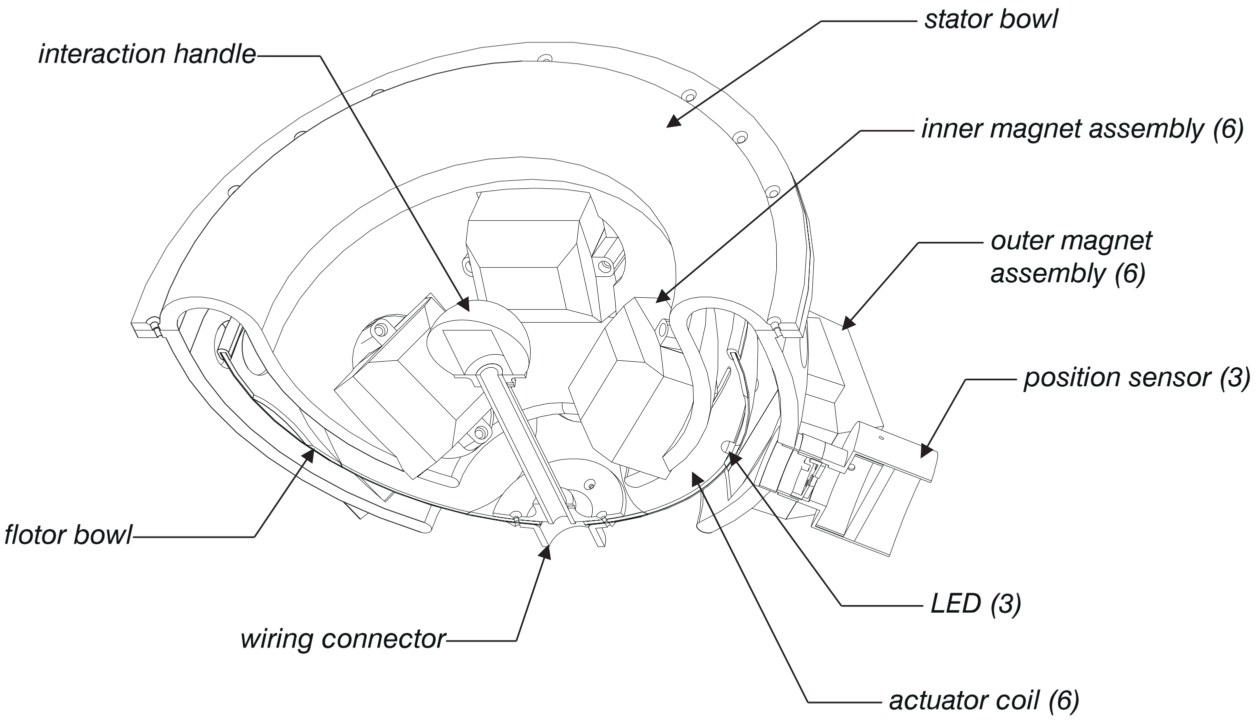

Figure 5: Cutaway View of the Haptic Device

motions, translation beyond typical fingertip motion for common tool-based tasks is less critical than the sensitivity and control bandwidths of the device.

Although the expanded motion range of the new device is large enough for fingertip motion, its utility would be severely limited if the user could only move the virtual tool over the same range in the simulated environment. To enable the user to move the virtual tool over larger distances in the simulated environment, variable scaling, position indexing, and rate-based control modes will be available to the user during interaction. These additional control modes will be described in section 9.2 with the user interface.

2.4 Handle

Depending on the tasks to be simulated, other handle shapes such as a stylus, joystick, or T-grip may be more suitable than the ball grip currently mounted on the flotor as shown in Figs. 4, 5, and 6. To enable the use of different handles, the current handle was designed to be easily replaceable. For the best correspondence between the device and the simulation, the tool handle shown in the virtual environment should be the same shape as the handle currently installed on the device flotor.

A number of additional handles will be built and evaluated for their suitability and ease of use with various haptic interaction tasks. Different handle shapes and their advantages and disadvantages are listed below:

ball handle: symmetrical, easy to grip, good for fine fingertip motion, but difficult for the user to apply high torques.

T-grip: best for large forces and torques, comfortable hand position, but not as good for dextrous fine motions.

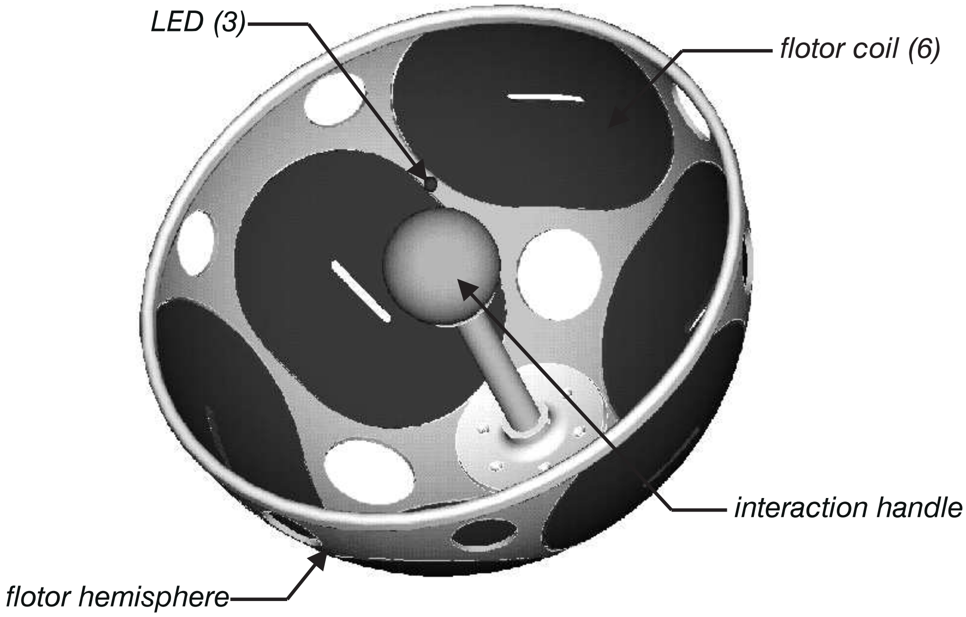

Figure 6: Hemispherical Flotor Shell with Coils, LEDs, and Handle

stylus: thin (pen) very good for fine tool manipulation, thicker handle is good for typical hand shop tools such a screwdriver or wrench.

joystick: familiar, responsive, accommodates added buttons or switches well.

Various buttons or switches can also be added to the handles so that the user can easily switch between different operating modes such as position or rate-based control, or initiate some action in the simulated environment such as grasping and release. A compact 6 DOF force sensor will also be added between the device handle and the coil hemisphere to enable inertial compensation, improve dynamic control accuracy, allow a wider variety of control algorithms, and provide more information to the simulation.

3 Actuation

As with the previous Lorentz maglev devices, NdFeB rare earth alloy permanent magnets were used for the magnet assemblies. The current maglev device uses the highest $B_{max}H_{max}$ energy product magnets available, with 48 MGOe maximum energy product.

3.1 Single Actuator

A single Lorentz force actuator consists of two opposing fixed magnet assemblies and an oval wound coil suspended between them in the magnetic circuit air gaps. The Lorentz force $\boldsymbol{f}$ on the coil is generated in the two air gaps where the coil current loop $\boldsymbol{I}$ intersects the magnetic flux loop $\boldsymbol{B}$ and

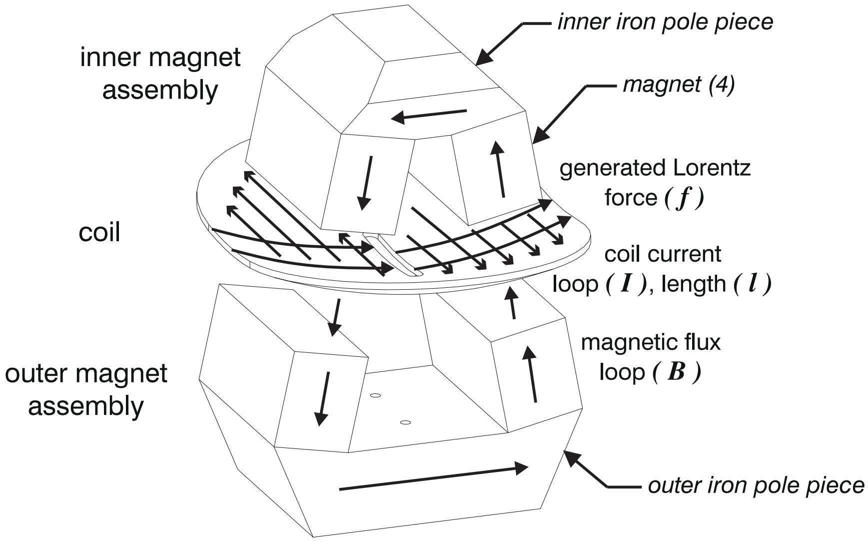

Figure 7: Single Actuator with Magnet Assemblies and Suspended Oval Coil

are perpendicular to both the current and the magnetic field vectors. A Lorentz actuator for the new device is shown in Fig. 7 with the associated vectors $\boldsymbol{f}$, $\boldsymbol{I}$, and $\boldsymbol{B}$.

The inner and outer magnet assemblies in the new actuators have different widths and the coil is spherically curved in order to conform to the overall hemispherical shape of the new device. Due to the curvature of the coil and the tapered shape of the magnet assemblies, the forces generated from the two sides of the coil are not in line with each other, although the vertical components of the generated forces cancel each other out. As a result, the net force generated from this actuator is slightly smaller than the force that would be generated from straight vertical magnetic fields and a perfectly flat coil of equal area, although the torque generated around the hemisphere center is greater than the one that would be generated from a flat coil.

Magnet assembly design was carried out using the Maxwell-3D field simulation finite element (FEA) analysis software package from Ansoft. A full three-dimensional FEA model was used rather than a simplified 2D one due to the high energy product of the permanent magnets and the large size of the air gap relative to the size of the magnets. The air gap between the inner and outer magnet assemblies is 32 mm to accommodate the thickness of the flotor, its range of motion, and its curvature. The magnet sizes are $20 \times 50 \times 25$ mm, to provide a field strength of 0.35 T at the center of the air gap using limited size magnets. The separation distance and angle between the two pairs of magnets in each assembly was determined by the size of the actuator coils and the range of motion of the flotor. A current of 2 A through each of the three rim coils when the flotor is in the center position is predicted to result in 60 N of vertical force. The flotor mass is 850 g with copper coils.

Because of the large air gap in each magnet assembly, the magnetic field varies from 0.2 T at the edge of the gap, to 0.35 T at the center, to 0.6 T by the faces of the magnets. Due to this variation, the Lorentz force obtained from the coil current is dependent on the position of the coil in the air gap. The force increases as the coil approaches the faces of the magnets and decreases as it moves sideways so that less of the coil is exposed to the areas of high magnetic field. I plan to compensate for the variations in the coil force magnitude by measuring the relation between current and force magnitude with a fixed force sensor throughout the range of motion of a coil and making a 2-D interpolated lookup table indexed by the two directions described which will be used to rescale the current to correctly

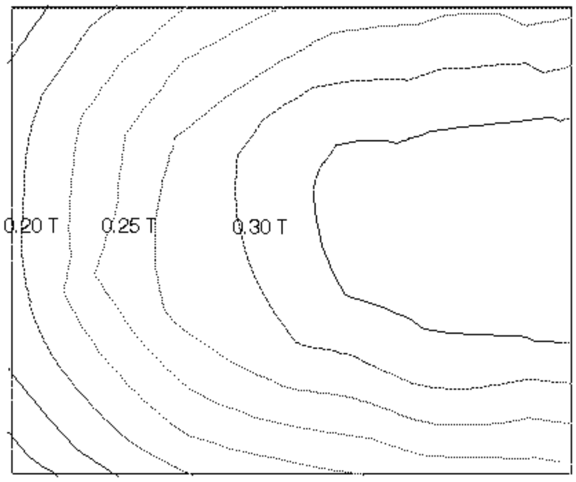

Figure 8: FEA Predicted Magnetic Field in Gap

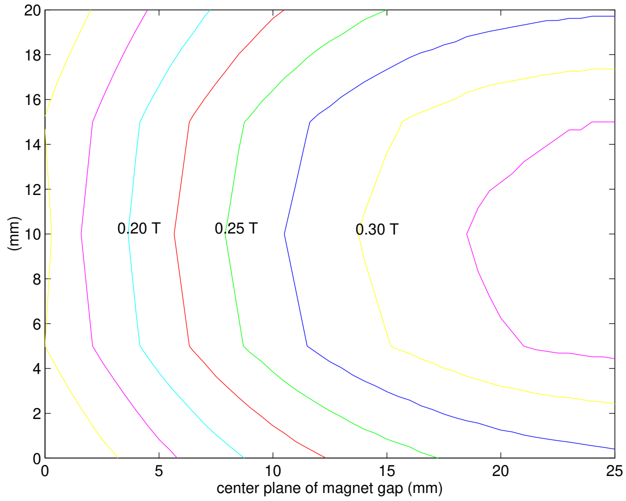

Figure 9: Measured Magnetic Field in Gap

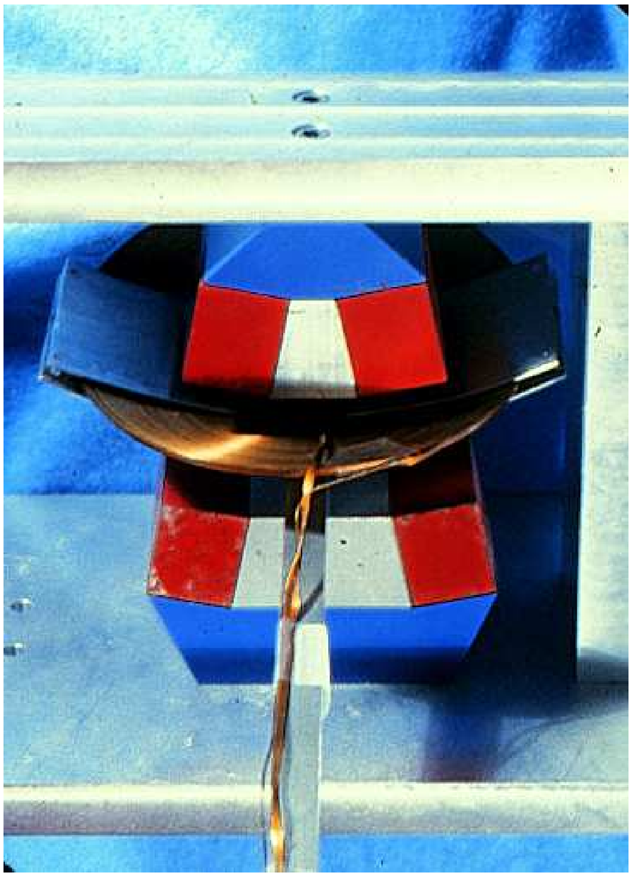

Figure 10: Test Actuator

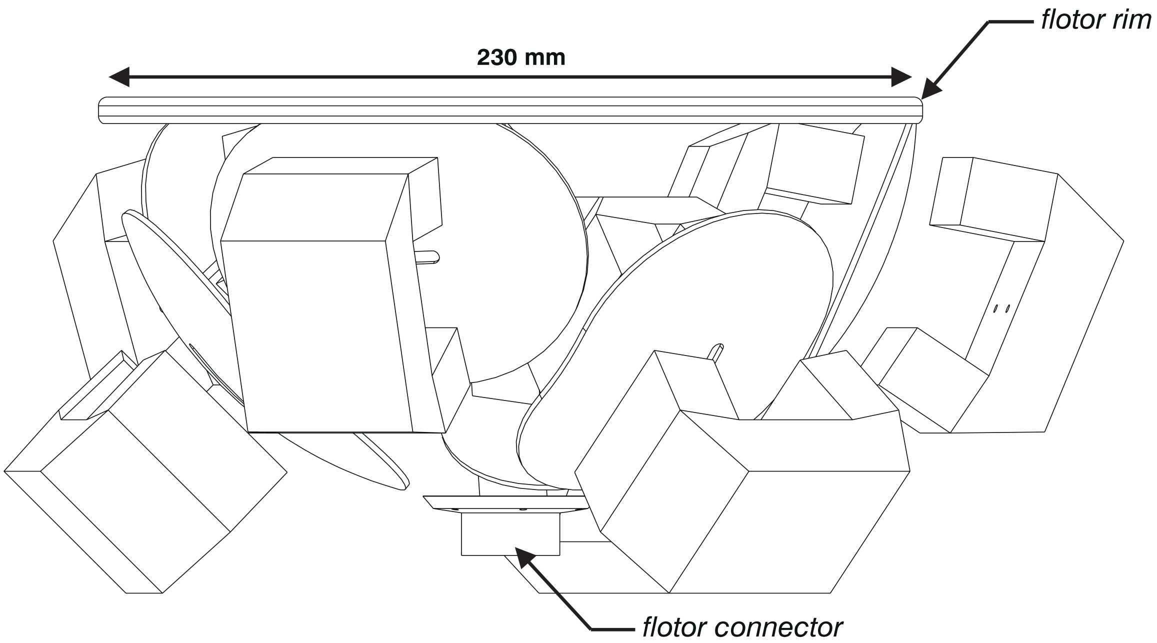

Figure 11: Configuration of Six Actuators

generate the desired forces.

The magnitude of the magnetic field in the center of the gap in the half-plane equidistant from the faces of the two magnets is shown in Figs. 8 and 9, where the plot shown in Fig. 8 is from FEA analysis and Fig. 9 is from actual gaussmeter measured values from a test magnet assembly. The prototype test actuator pictured in Fig. 10 generated 7.2 N/A rather than 8.0 N/A as predicted by the FEA results with the sample coil centered in the magnetic field gap. The 10% difference may be attributable to FEA errors and a coil winding less dense than expected.

3.2 Actuator Configuration

The configuration of the six actuators for the new device is shown in Fig. 11. The flotor hemisphere rim and pole connector are also shown for clarity. This tightly packed configuration results in high actuation force efficiency, large ranges of translation and orientation, and low inertia. The hemisphere area is used as much as possible for actuation, in order to maximize the force:inertia ratio of the device and, consequently, its motion bandwidth.

To efficiently generate forces and torques in all directions, the actuator magnets and coils are arranged with three actuators next to the hemisphere rim centered at 22.5° below the rim and the other three centered at 45° and rotated by 90°. The positions and orientations of the six coil centers on the hemisphere are listed in Table 2 and pictured in Fig. 12, where θ is the angular position from the x axis along the rim, ϕ is the angle down from the hemisphere rim, and ψ is the angle between the long axis of the coil and the hemisphere rim. Each oval-shaped actuator coil is curved to conform to the flotor shell and spans a $45° \times 61°$ solid angle on the hemisphere. The six oval-shaped flat actuator coils together occupy approximately two-thirds of the flotor area. The flotor shell radius of 115 mm results in large actuator surface areas and forces, yet allows the levitated mass to be easily manipulated and the entire device to be contained in a deskside cabinet enclosure. The outermost aluminum shell covering the coils adds passive damping to the motion of the flotor due to eddy currents generated by

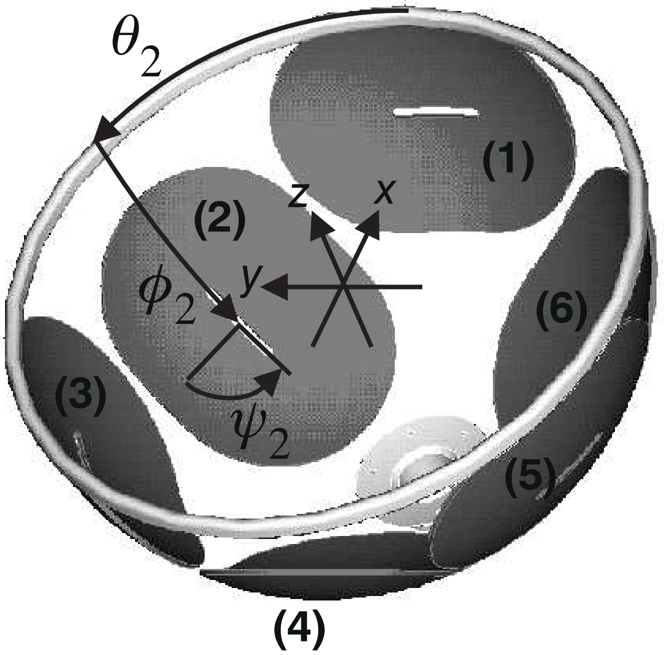

Figure 12: New Flotor Coil Configuration

motion through the strong magnetic fields in the stator magnet assembly gaps, which increases the range of stability of the controlled device.

The forces and torques generated on the flotor when it is in the centered position can be expressed as $\mathbf{F} = \mathbf{AI}$, where $\mathbf{F} = (f_x, f_y, f_z, \tau_x, \tau_y, \tau_z)$ is a 6-vector consisting of the forces and torques exerted on the flotor center, $\mathbf{I}$ a 6-vector of the coil currents, and $\mathbf{A}$ the matrix which maps them. $\mathbf{A}$ can be calculated by combining the sums of the Lorentz forces and torques

$$\mathbf{f_i} = \mathbf{I_i} \times \mathbf{B_i},$$

$$\tau_\mathbf{i} = \mathbf{c_i} \times \mathbf{f_i},$$

where B_i are the magnetic fields of each magnet assembly air gap and c_i are the coil center locations[24]. Small variations in the current-to-force transform matrix caused by changes in the directions of the coil forces depending on the flotor orientation will be neglected during operation.

The actuator configuration described above results in the transform matrix:

$$\mathbf{A} = \begin{bmatrix} 2.7553 & -6.2354 & -1.3777 & 0 & -1.3777 & 6.2354 \\ 0 & 3.6000 & 2.3862 & -7.2 & -2.3862 & 3.6 \\ 6.6519 & 0 & 6.6519 & 0 & 6.6519 & 0 \\ 0 & 0.2927 & 0.7171 & -0.5855 & -0.7171 & 0.2927 \\ -0.8280 & 0.5070 & 0.4140 & 0 & 0.4140 & -0.5070 \\ 0 & 0.5855 & 0 & 0.5855 & 0 & 0.5855 \end{bmatrix}$$

The matrix $\mathbf{A}$ determines the efficiency of force and torque generation in different directions. The top three rows determine generated forces and the bottom three rows determine generated torques.

Coil	Theta	Phi	Psi
1	0^o	22.5^o	0^o
2	60^o	45^o	90^o
3	120^o	22.5^o	0^o
4	180^o	45^o	90^o
5	240^o	22.5^o	0^o
6	300^o	45^o	90^o

Table 2: Coil Positions on Flotor Hemisphere

It is analogous to the transposed Jacobian matrix and the manipulability matrix for manipulators introduced by Yoshikawa[29]. To generate force and torque in arbitrary directions from a given coil configuration $\mathbf{A}$ must be nonsingular. Furthermore, the range of attainable forces and torques from a given maximum current for each coil describes ellipsoids whose principal axes are determined by the singular values of $\mathbf{A}$:

$$\mathbf{s} = [11.5215 \;\; 9.4984 \;\; 9.4984 \;\; 1.0141 \;\; 0.6867 \;\; 0.6867]$$

This vector indicates that the maximum horizontal forces are 82% of the maximum vertical force and that the maximum torques about the horizontal axes are 67% of the maximum torque about the vertical axis.

The steady-state vertical forces necessary to counteract the weight of the levitated flotor are distributed over the three coils next to the hemisphere rim so that the heat generated by the coil resistances is more easily dissipated. Heat dissipation in the actuator coils was a primary concern in the device design since the operating temperature of the coils is the limiting factor for the maximum steady-state forces exertable by the device. Due to this concern, the outer stator bowl was designed with air vents and thermistors were embedded in the flotor coils so that coil temperatures could be monitored during operation.

During preliminary testing of the finished device, however, only 13 W of power required to cancel gravity onthe flotor and the coil temperatures only slightly increased above room temperature. Since heat dissipation is less critical than anticipated, aluminum ribbon coils have become a more attractive option. Although aluminum has 50% more resistivity than copper, its density is only 30% that of copper. Since most of the mass of the flotor is in the coils, an aluminum coil flotor will have approximately half of the mass of the copper coil flotor, the power required to lift the flotor will be reduced by half, and the motion bandwidth of the entire device will be considerably increased. If the maximum position control bandwidth of the device is proportional to $1/\sqrt{m}$, then the bandwidth would be increased by $\sqrt{2}$ or 41%. Therefore, I plan to fabricate an aluminum coil flotor to replace the copper coil flotor used at present.

4 Sensing

Position is sensed by three lateral effect planar position sensitive photodiodes (PSDs) on the fixed outer stator which measure the positions of light spots from three LEDs mounted on the moving flotor. These provide six independent variables (x and y on each sensor) which together determine the position

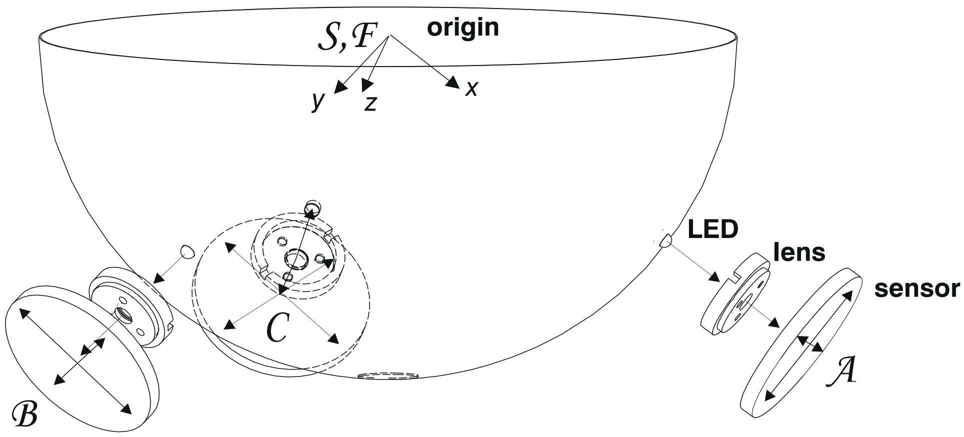

Figure 13: Sensor configuration and Coordinate Frames

and orientation of the flotor. The three sensors are equidistant from the stator center and mutually orthogonal to maximize position accuracy and simplify the geometric calculations. The sensor and LED configuration is shown in Fig. 13.

Due to the larger range of motion of the new device compared to the Magic Wrist and the UBC Wrist, a new position sensing scheme was designed. Instead of using narrow-beam LEDs shining directly onto the position sensing photodiodes, wide-beam LEDs on the moving flotor are imaged onto the photodiodes by fixed demagnifying lenses. Photodiodes sufficiently large and accurate to accommodate the range of motion of the new device with narrow-beam LEDs could not be obtained.

Sensor assemblies containing a lens, sensor, housing and a sum-and-difference signal conditioning circuit to be fastened to the outer stator bowl were designed by Zack Butler. A lens demagnification ratio of 1:2.5 at the nominal flotor position maps the full range of motion of the LED onto the limited area of the sensor. The sensor assembly and the light path of the LED is shown in Fig. 14. The x, y spot position on the sensor determines the angles between the light path and the lens axis, but the LED-lens distances must be calculated from all the sensor signals in combination.

Anti-aliasing filters with a 1000 Hz cutoff are used to condition the sensor signals sampled by the analog-to-digital converters.

4.1 Sensing Kinematics

The coordinate frames required for the forward kinematics are the fixed stator frame $\mathcal{S}$, the moving flotor frame $\mathcal{F}$, and sensor frames $\mathcal{A}$, $\mathcal{B}$, and $\mathcal{C}$ at each lens. $\mathcal{S}$ and $\mathcal{F}$ are coincident when the flotor is at its home position, as shown in Fig. 13.

The forward kinematics are computed by first finding the position of the LED in its corresponding lens frame with respect to the transformation matrix ${}^{\mathbf{s}}_{\mathbf{f}}\mathbf{T}$, which describes the flotor's motion. With the constant vector ${}^{\mathbf{f}}\mathbf{A}$ (the location of LED a with respect to the flotor frame) and the constant transformation matrix ${}^{\mathbf{a}}_{\mathbf{s}}\mathbf{T}$, this is given by

$$^{\mathbf{a}}\mathbf{A} = {}^{\mathbf{a}}_{\mathbf{s}}\mathbf{T}\, {}^{\mathbf{s}}_{\mathbf{f}}\mathbf{T}\, {}^{\mathbf{f}}\mathbf{A}.$$

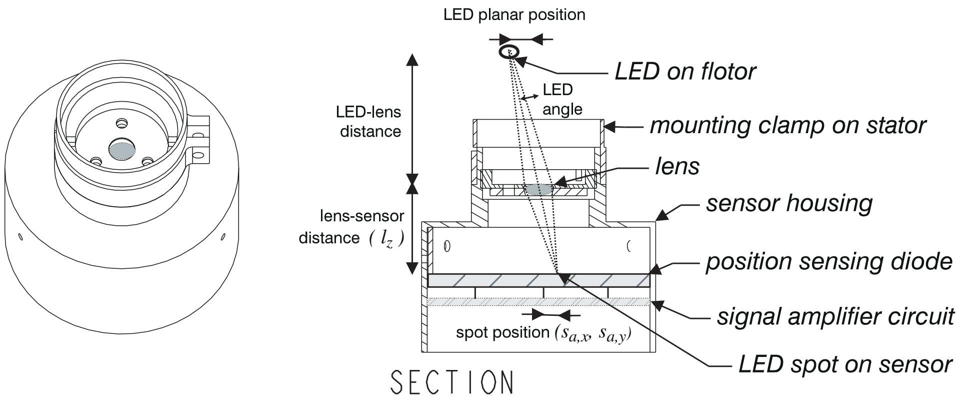

Figure 14: Sensor Housing

The light source is imaged on the sensor at a point given by

$$\begin{bmatrix} s_{ax} \\ s_{ay} \end{bmatrix} = \left(\frac{-l_z}{{}^aA_z}\right) \begin{bmatrix} {}^aA_x \\ {}^aA_y \end{bmatrix}$$

where l_z is the distance from the lens to the sensor (10 mm).

The 6-vector used for position is $\{n_1\theta\ n_2\theta\ n_3\theta\ X\ Y\ Z\}$, where n_1, n_2 and n_3 represent a normalized rotation axis, θ the rotation angle about this axis, and X, Y, and Z the translational motion of the origin. The rotation angle θ can be extracted from this vector by calculating the norm of elements $n_1\theta$, $n_2\theta$, and $n_3\theta$. Creating ${}^s_fT$ as a function of these variables and computing $s_{a,x}$ and $s_{a,y}$ from the equations above gives:

$$s_{a,x} = \frac{l_z l_l[n_1 n_3(1-\cos\theta) - n_2 \sin\theta] + Z}{l_l[n_1^2 + (1-n_1^2)\cos\theta] + X + l_z - l_t}$$

$$s_{a,y} = \frac{l_z l_l[n_1 n_2(1-\cos\theta) + n_3 \sin\theta] + Y}{l_l[n_1^2 + (1-n_1^2)\cos\theta] + X + l_z - l_t}$$

where l_l is the distance from the flotor origin to the LED (115 mm) and l_t the distance from the stator origin to the sensor (150 mm). The forward kinematics computations for the other two sensors are similar.

No closed-form solution for inverting the sensor signal formulas could be obtained, so iterative solution techniques are used. A fast numerical root-finding procedure formulated by Stella Yu using the motion history to obtain initial position guesses will be used to solve Cartesian position and orientation from the sensor signals in real time during device operation. The stator frame position and orientation can easily be converted to any other desired Cartesian control frame by using a homogeneous transform matrix.

The time required to calculate the position and orientation of the flotor in Cartesian space imposes the hardest limitation on the maximum cycle rate of the controller. Therefore, the speed of the kinematics solution is critical to the bandwidth performance of the device.

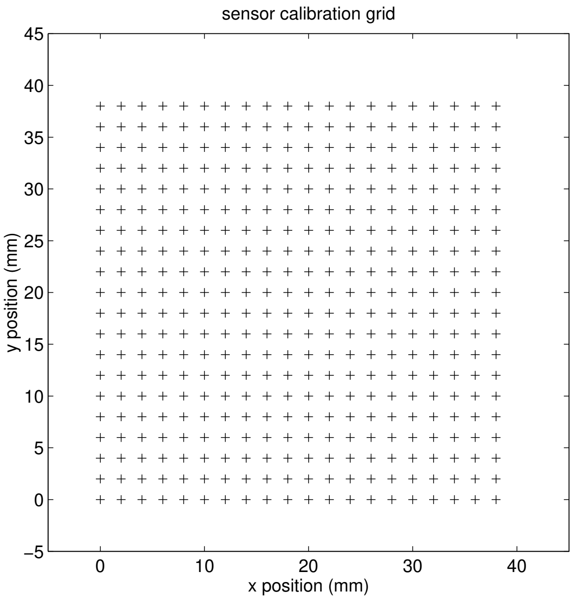

Figure 15: LED Position Calibration Grid

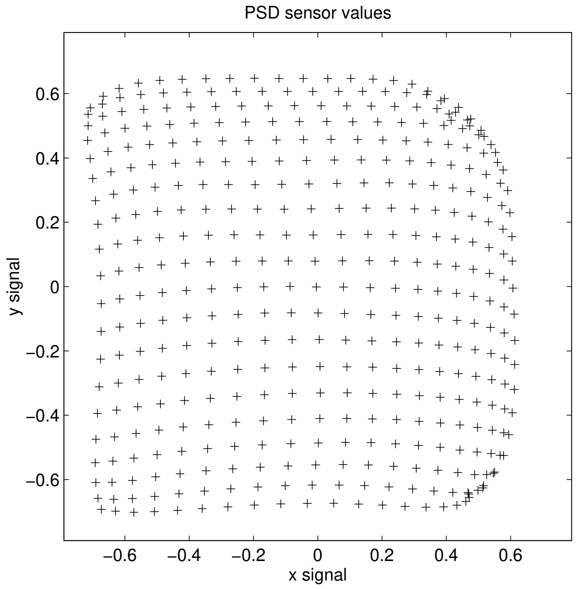

Figure 16: Sensor Signal Distortion

4.2 Sensor Calibration

Planar position sensing photodiodes operate by a lateral photoelectric effect. Light striking the surface generates an electric charge which is collected by electrodes on the four edges of the square device. The charge flowing to each electrode is approximately inversely proportional to the distance from the electrode to the light spot. The position of the centroid of the light spot on the sensor can thus be approximately calculated as follows:

$$\frac{x_{pos}}{L} \cong x_{signal} = \frac{x_1 - x_2}{x_1 + x_2}$$

$$\frac{y_{pos}}{L} \cong y_{signal} = \frac{y_1 - y_2}{y_1 + y_2}$$

where L is the distance from the center to each electrode and x_1, x_2, y_1, and y_2 are the currents through each electrode.

The PSD output signals have significant nonlinearities near their edges and offsets which must be corrected to achieve accurate position sensing over the range of motion of the device. The combined effects of physical misalignment, optical misalignment, and sensor zero point offsets cause the x and y readings from each sensor to vary from zero when the flotor is in the center position. In addition, there is warping of the sensor signals which becomes more pronounced towards the edges of each sensor. The signal to noise ratio of each sensor is also critical to the positional accuracy.

The sensors were calibrated by moving the LED over a 20×20 grid of points spaced 2 mm apart, 15 mm above each of the three sensor assemblies and measuring the x and y sensor output at each point. The nonlinear distortion of sensor A is shown in Figs. 15 and 16, where the planar grid of LED positions of Fig. 15 maps to the warped grid of sensor signal outputs shown in Fig. 16. The sensor nonlinearity at the extremes of this range of motion corresponds to a difference of approximately 5 mm in the LED planar position at the 15 mm height.

To accurately obtain LED spot positions given x and y sensor signals, a 2-D cubic reinterpolation (using Matlab) was done on each set of calibration data to obtain an inverted mapping from a regular grid of sensor values to the corresponding inversely warped grid of LED spot positions. The reinterpolated data sets will be used as lookup tables online during device operation to quickly calculate LED spot positions by 2-D linear interpolation at each sample period. Since the reinterpolated sensor values are spaced in a regular grid, the lookup tables can be indexed instantly rather than with a bisecting search.

5 Control

Feedback control in 6 DOF is necessary for stable magnetic levitation. Gravity compensation can be done with a constant feedforward term in the controller.

The forces exerted *by* the user's hand have a relatively low bandwidth of 10-20 Hz while the forces exterted *on* the hand by the device may have frequencies up to half the control rate, so a slow lowpass filter or estimator is sufficient to track the hand motion disturbances. The motions and forces of the user's hand are treated as disturbances by the controller and state estimator.

The digital control and kinematics computations for the device are to be executed by a VMEbus DSP board while a 68040 single-board computer handles communication, timing, and updating state variables. Ethernet UDP and TCP/IP socket connections enable communication with a graphics workstation host. With this setup, a complex physical simulation may be executed on the workstation host while the on-board processors for the device handle only local kinematics and compliant control computations. The separation of the simulation and the device control processing allows the device to easily be connected to any different workstation executing a different simulation. A dedicated fast serial connection could be also be used instead of the Ethernet connection for faster, more reliable communication without network traffic interference.

5.1 PD Control with State Observer

It is easiest and most straightforward to represent the orientation of the flotor about a given center of compliance with the Euler angles roll, pitch, and yaw or $(\theta_x, \theta_y, \theta_z)$ as the three independent variables to be controlled. If small angles and rotational velocities are assumed, then the flotor dynamics can be modelled as 6 decoupled second order systems. Unfortunately these assumptions overlook the coupled nonlinear aspects of spatial rotations, leading to errors in the spatial compliance resulting from the control system.

The simplest effective means to control the levitated flotor is by proportional-derivative error feedback gains. Physical mechanisms and rigid contacts can easily be emulated with PD control since the stiffness of the environment is given by the proportional error gain and the damping or viscous friction by the derivative feedback. Since flotor velocities are not directly measured by sensors, the velocities must be calculated from the calculated position history. Due to sensor noise, a well tuned estimator or filter should be used rather than straight numerical differentiation.

5.2 Spatial Impedance Control

A new method for controlling spatial impedance which is fully general and exact has been proposed by Fasse. The complete details and derivation of this method as well as theoretical and simulation results for magnetic levitation devices are given in [30]; an outline of this control method is given below.

The spatial impedance control algorithm generates feedback forces and torques for compliance, which is analogous to the single-axis proportional position error gain, and for damping, which replaces the derivative or velocity gain of PD control. The spatial compliance and damping are given by separate 3×3 matrices for translation, rotation, and translational-rotational coupling matrices. Coordinate frames in the control algorithm are given by homogeneous transform matrices containing a 3x3 rotation matrix $\mathbf{R}$ and a displacement vector $\mathbf{d}$. The relevant coordinate frames in spatial impedance control for a maglev device are:

- moving flotor frame $\mathbf{r}$ (described in section 4.1 as frame $\mathcal{F}$)
- virtual equilibrium frame $\mathbf{v}$, the flotor position and rotation setpoint which generates zero feedback forces
- center of stiffness frame $\mathbf{cs}$ defined relative to the flotor frame
- center of damping frame $\mathbf{cd}$ defined relative to the flotor frame

In the following stiffness feedback derivation, the $\tilde{\mathbf{q}}$ notation represents following matrix formed from the column vector $\mathbf{q} = [q_1\ q_2\ q_3]^t$:

$$\tilde{\mathbf{q}} = \begin{bmatrix} 0 & -q_3 & q_2 \\ q_3 & 0 & -q_1 \\ -q_2 & q_1 & 0 \end{bmatrix}$$

and the $\mathbf{as}$ operator returns the skew-symmetric part of a matrix. The $\mathbf{G}$ co-stiffness matrices are related to the $\mathbf{K}$ stiffness matrices and the principal axes of stiffness as follows:

$$\mathbf{G} = \mathbf{R\Lambda R}$$

$$\mathbf{\Gamma} = \mathbf{tr}(\mathbf{\Lambda})\mathbf{I} - \mathbf{\Lambda}$$

$$\mathbf{K} = \mathbf{R\Gamma R}$$

where $\mathbf{R}$ is a matrix of the principal axes of stiffness, $\mathbf{\Gamma}$ is a diagonal matrix of principal stiffnesses, and $\mathbf{\Lambda}$ is a diagonal matrix of principal co-stiffnesses.

For spatial stiffness feedback, the stiffness forces and torques are decomposed into translational, rotational, and coupling terms as follows:

$$\mathbf{f_{cr}} = \mathbf{f_t} + \mathbf{f_c} \text{ and } \mathbf{m_{cr}} = \mathbf{m_o} + \mathbf{m_c} + \tilde{\mathbf{d}}_{\mathbf{cs}}(\mathbf{f_t} + \mathbf{f_c})$$

where $\mathbf{f_{cr}}$ and $\mathbf{m_{cr}}$ are the total compliance forces and torques; $\mathbf{f_t}$ and $\mathbf{m_t}$ are the translational compliance forces and torques; $\mathbf{m_o}$ is the rotational compliance torque; $\mathbf{f_c}$ and $\mathbf{m_c}$ are the cross-coupling compliance forces and torques; and $\mathbf{d_{cs}}$ is the displacement of the center of stiffness frame from the flotor frame.

The translational force feedback is determined by a gain matrix and the center of stiffness frame transforms:

$$\mathbf{f_t} = \mathbf{R_{cs}^t K_t \Delta p}$$

where $\mathbf{\Delta p}$ is the displacement of the center of stiffness frame from the virtual equilibrium frame; $\mathbf{K_t}$ is the translational compliance matrix, and $\mathbf{R_{cs}}$ is the center of stiffness rotation matrix.

The rotational and cross-coupling forces and torques are given by:

$$\tilde{\mathbf{f}}_{\mathbf{c}} = \mathbf{2as}(\mathbf{R}^{\mathbf{t}}_{\mathbf{v}}\mathbf{G}_{\mathbf{c}}\mathbf{R}_{\mathbf{cs}}) \text{ and } \tilde{\mathbf{m}}_{\mathbf{c}} = \mathbf{2as}(\mathbf{R}^{\mathbf{t}}_{\mathbf{v}}\mathbf{G}_{\mathbf{c}}\boldsymbol{\Delta}\tilde{\mathbf{p}}\mathbf{R}_{\mathbf{cs}})$$

$$\tilde{\mathbf{m}}_{\mathbf{o}} = \mathbf{2as}(\mathbf{R}^{\mathbf{t}}_{\mathbf{v}}\mathbf{G}_{\mathbf{o}}\mathbf{R}_{\mathbf{cs}})$$

where $\mathbf{G_o}$, and $\mathbf{G_c}$ are the and the rotational and coupling compliance co-matrices; and $\mathbf{R_v}$ and $\mathbf{R_{cs}}$ are the virtual equilibrium and center of stiffness rotation matrices.

The damping forces and torques can be decomposed into rotation, translation and cross-coupling terms in a similar manner as the stiffness forces and torques:

$$\mathbf{f_{dr}} = \mathbf{f_{cd}} \text{ and } \mathbf{m_{dr}} = \mathbf{m_{cd}} + \tilde{\mathbf{d}}_{\mathbf{cd}}\mathbf{f_{cd}}$$

where $\mathbf{f_{dr}}$ and $\mathbf{m_{dr}}$ are the total damping forces and torques in the base frame; $\mathbf{f_{cd}}$ and $\mathbf{m_{cd}}$ are the total wrenches at the center of damping; and $\mathbf{d_{cd}}$ is the desired displacement of the center of damping frame from the end-effector or flotor frame.

The relations between the translational and angular velocities in the end effector or flotor frame and the center of damping frame are:

$$\mathbf{v^0_{cd}} = \mathbf{v^0_r} - \tilde{\mathbf{d}}_{\mathbf{cd}}\omega^{\mathbf{0}}_{\mathbf{r}} \text{ and } \omega^{\mathbf{0}}_{\mathbf{cd}} = \omega^{\mathbf{0}}_{\mathbf{r}}$$

where $\mathbf{v^0_r}$ and $\omega^{\mathbf{0}}_{\mathbf{r}}$ are the translational and angular velocities of the flotor and $\mathbf{v^0_{cd}}$ and $\omega^{\mathbf{0}}_{\mathbf{cd}}$ are the translational and angular velocities at the center of damping.

Given the translational and angular velocities at the center of damping, the feedback forces and torques at the center of damping can be calculated from the rotation and damping gain matrices:

$$\mathbf{f_{cd}} = \mathbf{R^t_r B_t v^0_{cd}} + \mathbf{R^t_r B_c}\omega^{\mathbf{0}}_{\mathbf{cd}} \text{ and } \mathbf{m_{cd}} = \mathbf{R^t_r B_c v^0_{cd}} + \mathbf{R^t_r B_o}\omega^{\mathbf{0}}_{\mathbf{cd}}$$

where $\mathbf{B_t}$, $\mathbf{B_o}$, and $\mathbf{B_c}$ are the translational, rotational, and coupling damping matrices; and $\mathbf{R_r}$ is the rotation matrix of the end effector or flotor.

For actuation of the Lorentz maglev device, the spatial impedance feedback forces and torques must be transformed into coil currents:

$$\mathbf{I} = -\mathbf{A}^{-1}\begin{bmatrix} \mathbf{f_{cr}} + \mathbf{f_{dr}} \\ \mathbf{m_{cr}} + \mathbf{m_{dr}} \end{bmatrix}$$

where $\mathbf{I}$ is the vector of coil currents, and $\mathbf{A}$ is the current-to-force transform matrix. Any feedforward terms to cancel gravity, changes in the location of the center of mass, or other force disturbances would also be added with the stiffness and damping force and torque terms.

This control method is general, exact and allows translational-rotational coupling at the center of compliance, which is not possible with the decoupled 6-axis PD control method. As it is correct and straightforward to apply, this spatial compliant control method will be implemented and used for control of the levitated platform.

During haptic interaction, the gain and transform matrices for spatial impedance will be recalculated on-the-fly to correspond to the points of contact between the haptic tool and other objects in the simulated environment at each sample period. Since it is fully general, this spatial control method will be able to represent any physically realizable rigid-body impedance that may be encountered in an interactive physical simulation. For interaction with rigid, polyhedral objects only, the full generality of the spatial impedance control method may not be necessary and the method could be simplified somewhat, for instance the center of damping frame may be kept coincident with the center of compliance since damping and stiffness are both generated from the points of contact.

Figure 17: Fabricated Flotor

6 Fabrication

The spherical curvature, complex part geometry, and cost considerations posed various problems in fabrication. Many parts were machined by CMU machine shops from Pro/Engineer drawings, but several parts had to be fabricated by hand in the laboratory at some point. All aluminum parts were black dye anodized[1] to minimize LED reflections and protect the surface finish.

6.1 Flotor

The flotor coils were wound in the lab using a coil winder while carefully controlling the wire feed speed, angles, and tension by hand. Convex and concave curved Teflon forms were used to conform each coil to the correct spherical curve and clamp it during epoxy curing.

The handle parts, connector socket, and flotor rim were machined by the CMU Mechanical Engineering machine shop. The aluminum hemispheres were formed by an outside vendor[2] by metal spinning on steel mandrels. The hole locations in the inner hemisphere were laid out in the lab using a (θ, ϕ) angular positioning setup, then fastener and LED holes were drilled, wiring and weight reduction holes were punched, and the large oval coil holes traced and cut by hand using nibbler tools. The two hemispheres were bonded together with vibration damping viscoelastic polymer adhesive sheet[3].

The coils were epoxied in place in the hemisphere with thermistors packed into their centers and the rim was attached to the hemisphere with thermally conductive epoxy. The LEDs were placed

[1] East Liberty Electroplating, Glenshaw PA.
[2] EH Schwab Co, Turtle Creek PA.
[3] 3M

Figure 18: New Fabricated Lorentz Levitation Haptic Device

with cyanoacrylate “krazy” glue. All flotor component wiring was done with flat ribbon wire to the connector at the pole of the hemisphere. The inside of the hemisphere was lined with adhesive bonded Teflon sheet to protect the wiring and coils from abrasion from contact with the inner stator bowl. For ease of assembly, the connector and its socket were attached to the hemisphere first, then the wiring pins were inserted into the connector from inside the hemisphere, then the handle parts were fastened to the hemisphere. The fabricated flotor is pictured in Fig. 17 before the Teflon lining was applied.

6.2 Stator

The iron pieces, magnet assembly aluminum braces, and the sensor housing pieces were machined from stock. The inner and outer stator bowls were first sandcasted[4] to near-net-shape with details machined afterwards to reduce fabrication costs.

Stator assembly must be done carefully because of the very strong magnets that must be handled. First, the magnet assembly iron pieces were bolted to the aluminum braces. Then, each magnet was guided into its assembly. The subassembly must be rigidly clamped while one person wearing gloves carefully puts the magnet in place and the other slowly pulls out the wooden wedge separating the iron from the magnet. The inner stator magnet assemblies were then placed and bolted to the inner stator bowl while using cardboard, tape and bubble wrap to guide positioning and prevent the magnets from coming too close to each other. The magnetic field directions must be the same for each set of magnets. The outer stator bowl and the inner stator were then bolted together with the flotor between them. The outer stator magnet assemblies could then be placed by hand without too much difficulty. The

[4] Laurel Aluminum Casting, Glassport PA

sensor housings and upper sets of magnets must be inserted into place after the device is placed in the enclosure since they will not fit through the hole in the enclosure desktop. The fully fabricated device outside of the desktop enclosure is shown in Fig. 18.

After the device assembly was completed, an unforeseen problem with the LEDs currently in use on the flotor became apparent: The casings of the LEDs are slightly ferromagnetic, which results in additional attractive forces on the flotor as the LEDs approach the magnetic fields of the actuators. These forces are disturbances which make the flotor motion more difficult to control accurately and reduce its closed-loop performance.

To eliminate this problem, non-ferromagnetic LEDs will be acquired for the new aluminum coil flotor to be fabricated. In the meantime, a position-dependent force feedforward term may be introduced to attempt to cancel the disturbance forces.

7 Current Status

Fabrication of the new maglev haptic device is now complete and the sensing and control systems are being tested, calibrated, and tuned for levitation. A preliminary iterative kinematics solution method proposed by Zack Butler has been successfully implemented. All necessary coordinate transformations between sensor and world position, coil currents and Cartesian forces and torques, and axis-angle to matrix and roll-pitch-yaw rotations have been implemented and tested.

The kinematics and control computations are currently being executed on the Motorola processor board only without using any additional DSP board, so the sample and control rates are limited to 500 Hz. With proportional control alone at that sample rate, the device is unstable in translation but stable in rotation at gains up to approximately 25 N-m/radian, due to greater passive damping during rotational motion. Current work progress is towards tuning sensor filters, velocity estimation, and control gains to achieve stiff, stable levitation.

8 Proposed Contributions

The proposed device is the first Lorentz maglev device that is specifically designed for haptic interaction. The expected control bandwidths for the device will be the highest yet achieved for any 6-DOF haptic interface device. The high performance of the device will provide an opportunity to better evaluate physical simulations, control algorithms, and integration methods. The results and conclusions of these evaluations will be applicable to any future haptic interface devices with similar performance parameters.

Reproducible Design: The device was designed to be easily reproducible. The complete design schematics are available and the procedures followed at each stage of fabrication of the device are well documented. Since low cost fabrication methods and materials were used, more devices of the same design can quickly and easily be fabricated for future research in other areas such as teleoperation and psychophysical perception. The materials, fabrication procedures, and components in the design are novel but not prohibitively expensive, such as the large PSDs, high energy NdFeB magnets, and spherical wound coils.

Evaluation: A thorough quantitative evaluation of the device performance parameters including the control bandwidths, accuracy, and ranges in both force and position will demonstrate the potential effectiveness of maglev haptic interaction in general and of the hemispherical design in particular.

The controlled bandwidths of the device will be measured with a dynamic signal analyzer and a force meter. The relative positioning accuracy will be measured with micrometer stages. The controlled force and motion ranges will also be measured with the micrometer stages and a force sensor or a set of gram weights.

Interactive Simulation Testbed: The magnetic levitation haptic interface device described here will serve as a testbed to investigate issues in high-performance haptic interaction with physical simulations. Since no other 6-DOF haptic interface device yet exists with the potential bandwidths of the new device, it will enable evaluation of richer, more subtle methods of interaction and simulation. The planned simulation methods and their integration with the haptic device are described in Part II of this document.

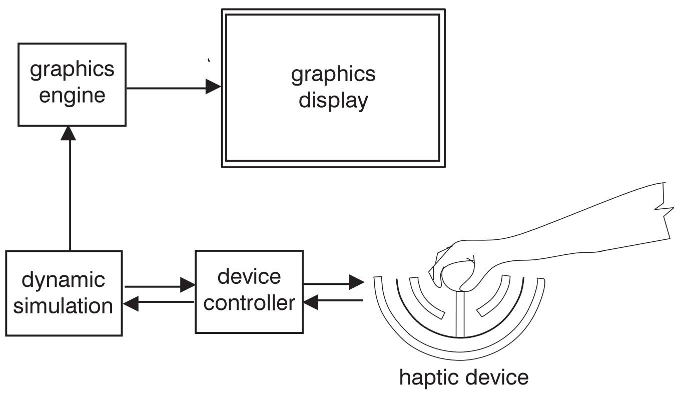

Figure 19: Haptic and Visual Interface System

Part II
Interaction with Simulated Environments

9 User Interface Additions

The second part of my proposed thesis work is concerned with user interface, simulation, integration, and evaluation aspects of the proposed haptic interface. Interaction with the haptic device alone would be an effective demonstration of the dynamic performance and realism of the device, but it would be of limited practical use for interacting with useful, meaningful simulated environments. In particular, the haptic interactive experience would be somewhat limited without a visual representation of the simulated environment and a natural way to move over large distances and angles within it. In order to give the user a more convincing, immersive experience and provide a means to move the haptic tool to any configuration in a simulated environment, it is necessary to add a realistic 3-D graphics display and additional interaction modes that the user can select for operation of the haptic device.

9.1 Graphical Display

The dynamic simulation environment during haptic interaction will be displayed using the OpenGL graphics library routines on a Silicon Graphics Indigo 2 workstation or, equivalently, using the MesaGL package on a Sun Sparc workstation. A schematic representation of the intercommunication between the device, controller, simulation, and graphical display systems is shown in Fig. 19. The physical simulation supplies data for the graphical display in real time as well as two-way interactive communication with the haptic device controller.

Haptic interaction and 3-D graphics complement each other very well since the combined interaction system recreates human visual/haptic interaction with real objects. Since human haptic perception of object shapes is distorted and inaccurate depending on the hand and arm position[31] and visual cues are dominant over haptic perception [32], small position and force errors in the haptic device control should not be perceived by the user during interaction if object shapes are also graphically displayed.

9.2 Control Modes

As mentioned in section 2.3, the size of the virtual environment should not be limited to the range of motion of the maglev device. The combination of different operating modes such as position indexing, variable scaling, and rate-based control will enable the user to move the virtual haptic tool easily over arbitrarily large distances in the virtual environment. When the virtual tool is in the desired local neighborhood, the user can then switch back to one-to-one correspondence between the virtual and actual forces and motions. The particular combination of control modes used to reposition the haptic tool will be up to the user. A control panel of sliders and buttons in the graphics display will allow the user to change and modify control modes during haptic interaction.

With variable scaling, the user will be able to scale spatial forces and positions to any range desired at any time. With position indexing, the user can set the current position of the virtual tool to correspond to the center position of the device whenever desired. This action in the 3-D haptic interface will be equivalent to picking up a 2-D mouse and repositioning it on the desktop or mousepad in order to increase its range of motion with a limited desk area and arm motion. It is hoped that position indexing with the haptic interface will be as automatic for users as with a computer mouse.

In rate-based control either the device position or the user-applied force on the device determines the velocity of the virtual tool. Although rate-based control cannot provide contact force feedback in a transparent way, satisfactory results have been obtained in teleoperation with a maglev device master by feeding back the derivative of the contact forces in the remote or simulated environment [33], so this force derivative feedback approach will be implemented on the new device in rate control.

10 Physical Simulation

I plan in the second part of my thesis work to build an integrated system to interact with realistic dynamic simulated environments using the described haptic interface device as a virtual tool. The previous implementations of magnetic levitation haptic interaction with simulated environments described in [26] and [27] were with a simple, limited static environment, in which only the wrist flotor (or haptic tool in the virtual environment) moved while the environment remained stationary. Although haptic interaction with a static environment is useful in itself to enable the user to feel the shape and surface characteristics of an object, the currently proposed work aims to provide interaction with a realistic physically simulated world in which objects dynamically react to forces acting on them due to collisions, friction, or force fields such as gravity or electromagnetism. Such a realistic, dynamic virtual environment, integrated with the haptic interface device controller described in Part I and a realistic graphical display, will provide users with a very convincing experience of directly interacting with physically real objects in a real environment.

To realize this type of interaction, a simulation engine is needed to model the behavior of objects in the virtual world in real time. In the proposed system, the simulation will execute on a workstation and communicate with the maglev haptic device controller via an Ethernet or fast serial cable link. The simulation software must continually and smoothly handle collision detection, object motion mechanics, contact forces, and communication with the device controller. The device controller will calculate and continually update its force feedforward and spatial impedance control parameters according to the contact state of the haptic tool in the simulated environment.

10.1 Physically-Based Modeling

The physically-based modeling systems developed by Baraff will be used to calculate forces and motions of rigid bodies in space due to Newtonian mechanics in real time on a graphics workstation. These algorithms calculate object dynamics by numerical integration of the environment model differential equations at each timestep, accounting for instantaneous collisions and motion constraints due to resting or sliding contact [34, 35]. A sample display of Baraff's real time physically-based simulations is shown in Fig. 20.

Three types of motion dynamics must be modelled: free rigid-body dynamics, collisions, and constrained motion such as sliding or resting contact. Free rigid body dynamics are straightforward to calculate given each body's state vector, initial conditions, and inertial parameters. Contact forces between objects are calculated from the relative velocities, the contact point, and a surface normal. Plane-to-plane and edge-to-plane contacts are modeled as multiple vertex-to-plane contacts. Vertex-to-vertex and vertex-to-edge contacts are degenerate and can be treated as vertex-plane contacts, since they can only occur instantaneously. For edge-to-edge contacts the surface normal is defined to be perpendicular to both edges.

In this simulation approach, objects are assumed to be perfectly rigid and non-interpenetrating. To prevent interpenetration when contacts occur, the necessary forces to prevent interpenetration are analytically computed and introduced into the simulation. In the case of collisions, the impulsive forces and accelerations are instantaneous. Since differential equation integration methods assume continuous dynamics, integration must be halted at the time of a collision and restarted again with new initial conditions.

Objects in prolonged contact with one another are subjected to only continuous forces and accelerations so discontinuities in the dynamics integration are unnecessary. Since the contact forces for multiple contacts may depend on each other, they must all be computed simultaneously. These forces must be solved using a quadratic program, however the parameters of the problem are such that this quadratic program can be solved efficiently.

Collision detection to prevent interpenetration can be a computationally intensive requirement of the physical simulation. A naive method of comparing points and faces at each time step would require $O(n^2)$ computation; efficient updating of a dependency tree structure can considerably reduce the computation required in practice. A 3-D hierarchical bounding box approach is reported to run essentially in $O(n + k)$ with k the number of pairwise bounding box overlaps [34].

10.2 Friction

Introduction of Coulomb friction into the non-penetrating rigid-body physically-based simulation could require exponential computation time, but a reformulation allowing additional introduction of non-impulsive contact forces enables the use of algorithms with polynomial time behavior [36].

Viscous friction or damping in the maglev device dynamics is produced by the derivative gain in the controller applied to filtered or estimated velocities. Previous work has shown this method to be especially effective in emulating damped collisions, sliding on sticky or oily surfaces, and motion of objects submerged in viscous fluids, provided that the velocity filter or estimator described in section 7.1 is tuned to eliminate inaccuracies from sensor noise and quantization effects but still capture the motions of the user's hand and fingers.

The emulation of dry sliding or *Coulomb* friction is slightly more involved as it requires monitoring and updating a stick/slip condition. When a virtual tool object surface is in contact with another surface, the following algorithm determines motion on that surface [27].

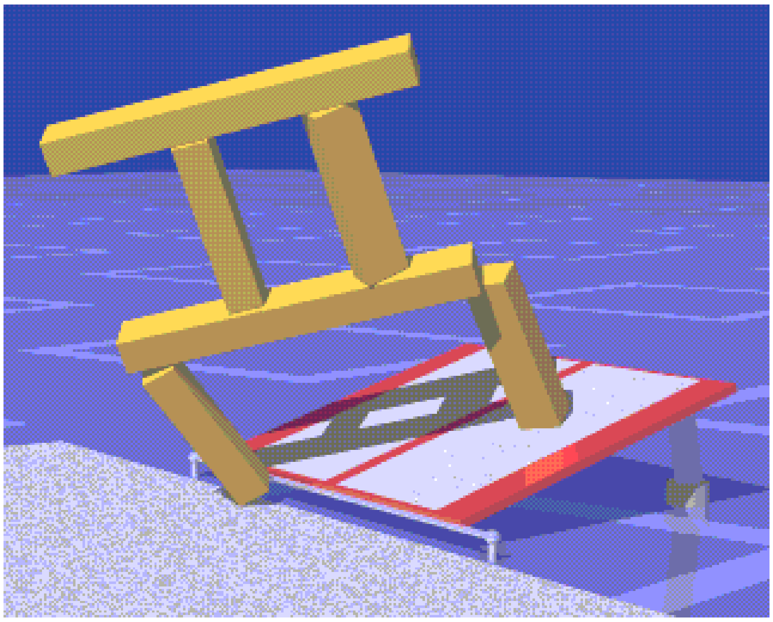

Figure 20: Sample Display of Physically-Based Simulation

During the sticking state, the control law used is:

$$f = -k_v \dot{x} - k_p(x_d - x)$$

If f exceeds a threshold force f_f, then the controller switches to the sliding state and uses the viscous only control law:

$$f = -k_v \dot{x}$$

When f falls below f_f again, the position setpoint x_d is reset to x and the controller switches back to the sticking state. The sliding force threshold is determined by the defined coefficient of friction μ between the surfaces and the normal force between the objects f_n according to Coulomb friction:

$$f_f = \mu f_n$$

Both types of friction have been demonstrated by the author [26] with a static environment using the IBM magic wrist. Implementation is straightforward and leads to a high degree of perceived realism in the haptic interaction. The integration of these friction emulation techniques with realtime physically-based modeling simulations will be an important result of this research work.

10.3 Texture

Convincing, realistic haptic display of texture was first demonstrated in the "sandpaper system" [37] with a 2-DOF force-reflecting joystick. Surface roughness was shown even with only 2 DOF in the plane by generating forces proportional to the local gradient of a simulated bumpy surface as shown in Fig. 21(a).

Surface texture was emulated with the Magic Wrist by defining a multifaceted surface and treating interaction with that surface in the same way as with other rigid surfaces[26]. A flat surface with parallel sawtooth grooves 200 μm wide and deep was defined as in Fig 21(b). Contact with the angled

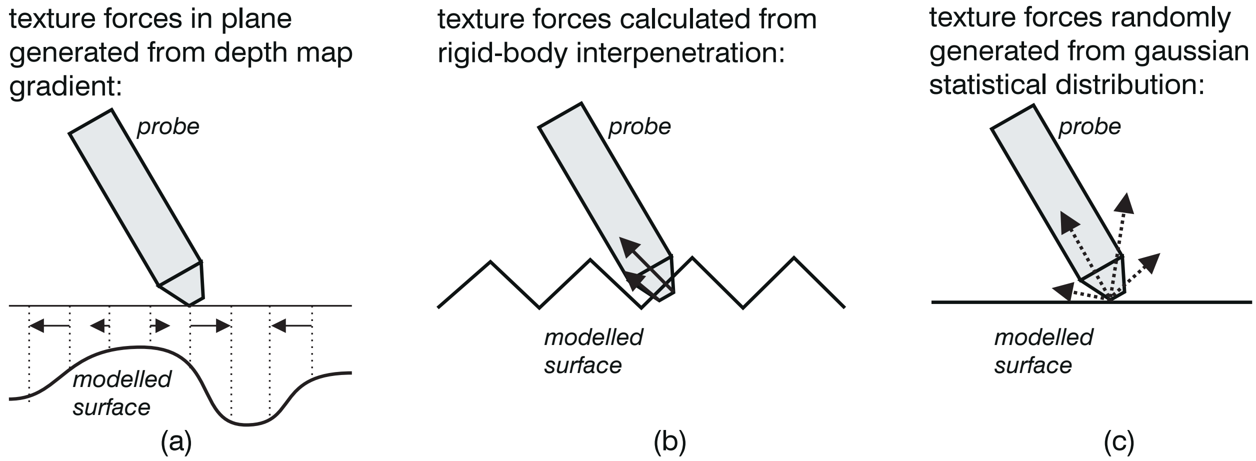

Figure 21: Texture modelling methods (a) Sandpaper system (b) surface grooves (c) stochastic

walls of the grooves produces a reaction force normal to the surface proportional to the interpenetration distance. A disadvantage of this method is the "pop-through" effect: The reaction force is calculated by the distance between the actual position of the flotor and the closest surface point, so the assumed surface contact point can "pop-through" from one side of a peak to the other. This phenomenon can be avoided by tracking "ghost" points on the surface during the interpenetration so that the force direction does not abruptly switch from one surface to another in a nonphysical way[38, 39, 40].

The presence of the grooves could be felt by the user through the Magic Wrist as long as the surface was sufficiently stiff. A buzzing sensation was felt as the flotor was moved perpendicular to the texture grooves, while the motion felt smooth parallel to the grooves. The addition of static friction improved the natural feel of the interaction.

For fine textures, pseudo-random generated force patterns will be superimposed on the contact forces, as in Fig. 21(c), to give the impression of surface textures instead of modelling surface features physically. A stochastic method of texture emulation for haptic interaction is presented and implemented in [41]. For texture emulation that is both realistic and efficient, the limitations of physical dynamics modelling, computational power, and human haptic sensing capabilities must be balanced against each other. In the proposed haptic interaction system, large shape features will be physically modelled, while smaller effects will be treated in an aggregate manner with stochastic/statistical texture generation methods. Below a certain size of shape detail, the increase in the complexity of the physical model and the amount of necessary information transfer between the simulation and the controller becomes prohibitively large as it approaches the limits of human tool-based haptic perception.

This surface texture simulation method for haptic display is analogous to 3-D graphics display methods: Larger geometric features are modelled with polygon meshes or spline curves, while fine texture patterns are directly mapped onto surfaces. For the best correspondence between the graphical display and haptic sensing of a virtual environment, the haptic texture can be either generated from the graphic texture or both the graphic and the haptic texture representations can be generated from an underlying surface roughness model in a manner similar to the "sandpaper system".

Synthesis or coordination between friction and texture emulation can improve the effectiveness and realism of haptic interaction, as the same physical effects of surface variations and microcollisions cause both texture and friction. Coulomb friction itself is an approximate model which averages out the effects of microscopic surface variations. Massie defines a "haptic spectrum": Real-world surface variations are haptically perceived as shape, texture, or friction according to their scale, or “wavelength” [38].

Dynamic and static Coulomb surface friction as well as texture is emulated in [42] by Mark *et al.* by a surface populated by snags in a model similar to the bumpy surface texture model of [37]. In [41], friction and texture emulation forces are completely decomposed so that

$$F_{contact} = F_{constraint} + F_{friction} + F_{texture}$$

The proposed haptic interaction system will use decomposed models of texture and friction for increased flexibility and simplicity in surface modeling, although more integrated friction and texture emulation models will be implemented so they may be evaluated.

An interesting feature of the haptic interface is that exotic physical effects are possible. For example, directionally dependent viscosity can be easily obtained by using different velocity feedback gains in each control axis.

11 System Integration

The effectiveness of the proposed haptic interaction system will depend on the system integration and virtual object control methods as much as on the dynamic performance of the device and the accuracy of the physical simulation. The intention of the integration methods is to make the haptic interface as transparent and direct as possible, so that the user can feel he or she is actually directly physically interacting with the simulated environment.

11.1 Simulation and Device Correspondence

The most critical problem that must be resolved to integrate physically-based modeling with the maglev haptic interface device is to maintain the correspondence between the simulated environment, the haptic interaction device, and the graphical display. The graphics display and the haptic interaction must be kept closely synchronized with minimal latency between them so that the environment seen in the display and felt through the device seems consistent and natural to the user. Perceptible differences in the feel and appearance of surface shapes or the timing of collision events seriously degrade the effectiveness of interaction with the simulated environment. To preserve consistency in the interaction system, the state information in the haptic device controller and the haptic tool object in the simulation must be mutually updated often enough that slight differences in timing, shape, and contact configurations will be overlooked by the user. For the best system performance, the simulation processing and the device control will be executed on separate processors and a local intermediate representation will be periodically generated by the simulation and communicated to the device controller to determine the device's spatial impedance at the much faster control cycle rate.

The simulation processing and device control must be decoupled because of their different performance requirements: The physical simulation requires very intensive processing and its update rate depends on the complexity of the environment and dynamic events occurring from moment to moment. A moderately complex simulation and graphical display executing on a SGI workstation updates at 20-30 Hz, which is sufficiently fast to appear almost continuous when graphically displayed to the user. The device controller must cycle at a much faster fixed sample rate, at least 500 Hz for convincing interaction with solid objects and preferably over 1000 Hz for realistic emulation of more finely detailed subtle surface characteristics. Rather than attempting to integrate intensive asynchronous computation, graphical display, I/O, and fast realtime sensing and control on a single processor, it is more practical and flexible to execute the realtime control task and analog I/O on a separate processor system.

Due to this decoupling, an intermediate dynamic representation will be used to achieve adequate performance. To keep the simulation and device control mutually consistent given limited communication speed and bandwidths, the simulation will periodically send a description of the local environment to the device controller. The device controller will calculate the control gains, setpoints, and compliance frame variables for spatial compliance control from the local environmental description of motion constraints supplied by the simulation. Dynamic events can then be predicted by the device controller so that they occur nearly simultaneously in the simulation and the actual dynamic behavior of the haptic device. The device controller must also return the flotor motion and actuated interaction force and torque back to the simulation so that the simulation responds to the user motion and forces.

Intermediate representation for virtual environment interaction was developed by Adachi *et al.* in [43]. Mark *et al.* in the UNC group describe several intermediate representations implemented there, including plane-and-probe; friction and texture; and multiple planes, probes, and springs [42].

A physically-based dynamic simulation has been integrated with a PHANToM 3 DOF point-based haptic interface device by Vedula with added Coulomb friction [44]. The most successful intermediate representation implemented consisted of a kinematic description of the object plane closest to the location of the probe tip in the virtual world including its updated position and the relative position and linear and angular velocity of the object's center of mass.

Previously developed intermediate representations [43, 42, 44] represent point force interactions only. For rigid-body 6 DOF haptic interaction, a more flexible and detailed intermediate representation is necessary. In the proposed research, I plan to develop a new representation model which will be able to generate and display complete force-torque wrenches resulting from all rigid body interactions. better

11.2 Intermediate Representations for Haptic Tool Contacts

The simplest way to extend point-contact intermediate representations for rigid-body interaction would be to generate representations for multiple contact points as suggested in [42]. The combination of the point forces would produce a force-torque wrench on the haptic tool in the simulated environment and be felt by the user. The drawback of this method is that it only emulates contacts between vertices of the haptic tool and planar surfaces in the simulation; edge-to-edge contacts and contacts between haptic tool planes and environment vertices would not be detected and would not generate reaction forces.

To emulate real rigid-body haptic interaction, the multiple-point representation method of [42] must be extended to recognize edge-to-edge and tool-plane-to-world-vertex contact forces also. A full intermediate representation for rigid-body contacts may become rather large even for simple objects, as illustrated by the cube alignment task of Fig. 22. Small perturbations in the position of the cube shown may result in any of the following rigid-body contacts:

- Point $\boldsymbol{A}$ with Plane $\boldsymbol{abcd}$, $\boldsymbol{acge}$, and $\boldsymbol{abfe}$
- Point $\boldsymbol{B}$ with Plane $\boldsymbol{abcd}$ and $\boldsymbol{abfe}$
- Point $\boldsymbol{C}$ with Plane $\boldsymbol{abcd}$ and $\boldsymbol{acge}$
- Point $\boldsymbol{D}$ with Plane $\boldsymbol{abcd}$
- Point $\boldsymbol{E}$ with Plane $\boldsymbol{acge}$ and $\boldsymbol{abfe}$
- Point $\boldsymbol{F}$ with Plane $\boldsymbol{abfe}$
- Point $\boldsymbol{G}$ with Plane $\boldsymbol{acge}$
- Point $\boldsymbol{d}$ with Plane $\boldsymbol{ABCD}$
- Point $\boldsymbol{f}$ with Plane $\boldsymbol{ABFE}$

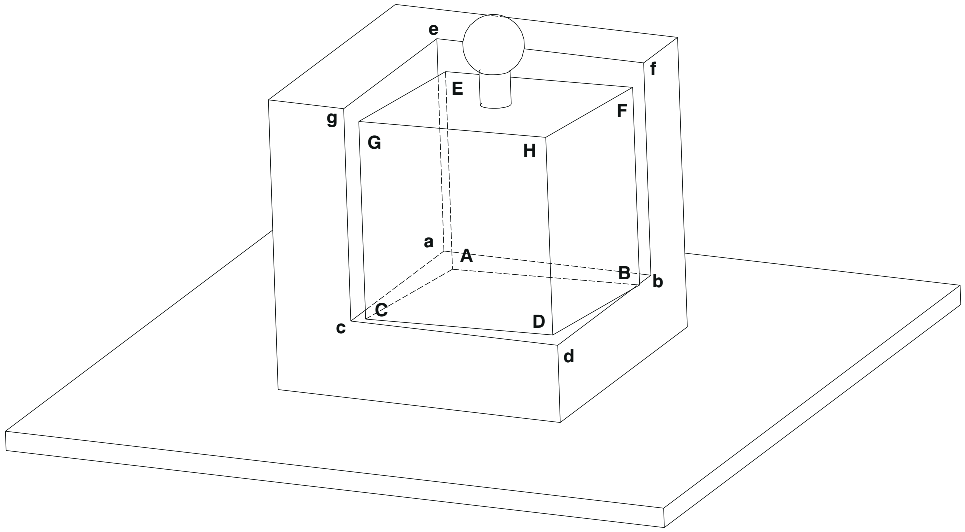

Figure 22: Potential Contacts Aligning a Cube

- Point $\boldsymbol{g}$ with Plane $\boldsymbol{ACGE}$
- Edge $\boldsymbol{AB}$ with Edge $\boldsymbol{bd}$ and $\boldsymbol{bf}$
- Edge $\boldsymbol{AC}$ with Edge $\boldsymbol{cd}$ and $\boldsymbol{cg}$
- Edge $\boldsymbol{AE}$ with Edge $\boldsymbol{ef}$ and $\boldsymbol{eg}$
- Edge $\boldsymbol{BD}$ with Edge $\boldsymbol{bd}$ and $\boldsymbol{cd}$
- Edge $\boldsymbol{CD}$ with Edge $\boldsymbol{bd}$ and $\boldsymbol{cd}$
- Edge $\boldsymbol{BF}$ with Edge $\boldsymbol{bf}$ and $\boldsymbol{ef}$
- Edge $\boldsymbol{EF}$ with Edge $\boldsymbol{bf}$ and $\boldsymbol{ed}$
- Edge $\boldsymbol{CG}$ with Edge $\boldsymbol{cg}$ and $\boldsymbol{eg}$
- Edge $\boldsymbol{EG}$ with Edge $\boldsymbol{cg}$ and $\boldsymbol{eg}$

For the intermediate representation to correctly represent this local object configuration, it must contain the positions and types of all the potential local contacts, as well as the translational and angular velocities of the relevant surfaces, edges, and vertices. Due to the limitations in communication bandwidth and processing speed for realtime force interaction, it may be necessary to limit the number of vertices and edges of the modelled haptic tool.

11.3 Integrating Intermediate Representations with Spatial Impedance Control

The impulsive collision forces and the intermediate representation contact states calculated by the simulation must both be introduced into the haptic device control in a physically realistic manner. The impulsive collision forces from the simulation will be reflected directly to the user while the local contact information contained in the intermediate representation will be used to calculate the spatial impedance gain and transform matrices. Generation of the spatial impedance control parameters from the intermediate representation and the flotor position must be done continuously and in real time to display realistic, dynamically changing contact states to the user. A fast algorithm to derive spatial impedance control parameters from the haptic tool position and the rigid-body intermediate representation will be formulated and implemented. The intermediate representation generated by the simulation processor may also include a partition of the configuration space of the haptic tool and precomputed spatial impedance control parameters in order to reduce the computational requirements of the fast realtime control system.

Collision forces from the dynamic simulation, interaction forces from the spatial impedance controller and the intermediate representation, and the friction and texture forces as described in the previous section will all be superimposed to give the user the most realistic haptic interaction with the physically simulated environment.

11.4 Simulation and Controller Integration Summary

To summarize the proposed integration of the physically-based simulation and the maglev device controller, the interactions between the simulation and the controller during free tool motion, tool-environment collisions, and constrained tool motion modes are described below:

Free tool motion: The physical simulation and the haptic controller are independent of each other in this mode. The user feels the actual inertia of the maglev flotor but the weight that is felt is dependent on the amount of feedforward gravity cancellation in the controller. The passive eddy current damping in the maglev device may be mostly eliminated if desired by adding negative damping in the control feedback. A collision detection algorithm executing with the physical simulation will signal any change to the free motion of the maglev flotor.

Tool-environment collision: When a tool-to-environment collision occurs, a collision force-torque impulse wrench is generated by the physical simulation, which is dependent on the masses and moments of inertia of the tool and the collided object, their relative velocity, and a predefined coefficient of restitution ϵ where $0 < \epsilon < 1$. The collision impulse vector from the simulation is communicated to the device controller and reflected to the haptic interface user at the right instant by applying a force $\mathbf{F} = \mathbf{J}/T$ to the flotor for one sample period, where $\mathbf{J}$ is the impulse vector and T is the sample period time. An equal and opposite collision impulse is introduced into the environment simulation dynamics. For the simple case where the flotor of mass m represents a point mass tool colliding with an stationary infinite-mass object, with a velocity v parallel to the surface normal, the collision impulse is $\mathbf{J} = -\epsilon m\mathbf{v}$.

Tool-environment resting contact and constrained motion: This is the most difficult case to emulate since arbitrary combinations of contacts must produce the correct spatial impedance for the haptic device flotor at each controller sample period. To accomplish this, an intermediate representation structure is sent to the device controller from the simulation containing position and velocity data for all potential contacts between the environment and the haptic tool, and possibly a partition of the haptic tool configuration space with precomputed impedances, until the next iteration of the simulation. The haptic device controller will then synthesize the correct spatial impedance for the haptic device flotor at each sample period of the device controller as different contacts are made and broken. The contact forces between the tool and the environment will be integrated until the next simulation sample period, when they will be communicated back to the simulation and introduced into the simulation dynamics.

The three modes of interaction are not independent but may run concurrently in some dynamic conditions. For example, one corner of the haptic tool may be in resting contact with an object in the simulated environment when a different corner of the tool collides with an object. The remaining unconstrained degrees of freedom of the haptic tool and flotor will have free motion to pivot around the constrained corners.

12 Evaluation

The haptic interaction system will be evaluated by experiments with a representative number of users executing predefined tasks in the simulated environment. The quality of the haptic interaction will be judged by the reliability and speed of task execution, comparison with execution of the same tasks with using real-world objects, and by the subjective impressions of the users regarding the realism of the interaction.

12.1 Evaluation Tasks

Representative tasks will be set up in the simulated environment as examples to demonstrate and evaluate the effectiveness and realism of the haptic interaction system. First, a simple "blocks world" environment will be set up to evaluate interaction for tasks with generic, simple objects. The second environment will be set up to demonstrate and evaluate the performance of a specific task such as inserting a key into a keyhole to push a sliding bolt open and shut, as shown in Figs. 23 and 24. Friction emulation is necessary in these tasks to prevent parts from sliding away and texture enhances the realistic feel of the surface contacts.

The"blocks world" environment will contain several polyhedral blocks and a virtual haptic tool with a shape similar to a forklift or backhoe scoop that will enable the user to push, align, and pick up arbitrary objects, as pictured in Fig. 25. The edges of the block models will be chamfered so that they can be picked up with the sharp edge of the scoop. The effectiveness of the haptic interface will be judged by how easily the users can push, stack, and otherwise manipulate the blocks to arrange them into structures.

Fitting one part into another is a common and general haptic task which encompasses CAD assembly, peg-in-hole, and molecular docking tasks. The interactions between 3-D rigid parts fitting together cannot be fully represented by any haptic devices with fewer than 6 DOF and a visual display alone cannot convey the subtleties of feeling parts contact and fit. Evaluation of the practicality of the haptic interface system will focus on the simulation of these kinds of tasks.

The key insertion and bolt sliding task will be modelled and implemented with the haptic interface and physical simulation systems to demonstrate the use of the system in simulating part fitting tasks. The haptic tool in this task will be the key itself which the user grasps and manipulates to insert it into the keyhole and slide the bolt back and forth. In this task, the objects in the simulated environment are only partially visible in the graphical display, since the inside of the lock and bolt contacted by the key are hidden from view. The user is able to position and insert the key visually but must use haptic perception to slide the key inside and push the bolt open or shut. This situation could also arise in a complex internal CAD assembly where small, complex fitting parts are hidden from view. The addition of different friction and texture characteristics to the surfaces in this simulation can enable the user to feel whether the surfaces are rough or smooth; oily, sticky, or rusty; and with regular or random textures.

12.2 User Evaluation

The realism and effectiveness of the interaction can be directly measured by comparing execution of simulated tasks to identically constructed real ones. The tools and objects modelled in the two described environments will be fabricated and assembled to be identical to the simulated environment so that execution of tasks in the real world and in the simulated environment can be directly compared.

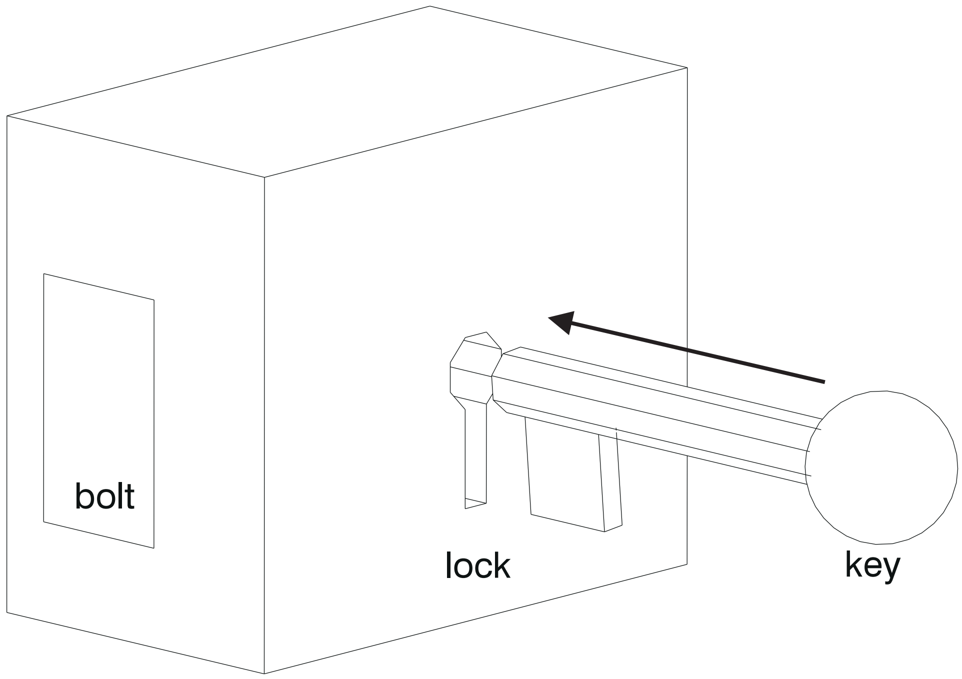

Figure 23: Sample 3-D Haptic Task: Key Outside Lock

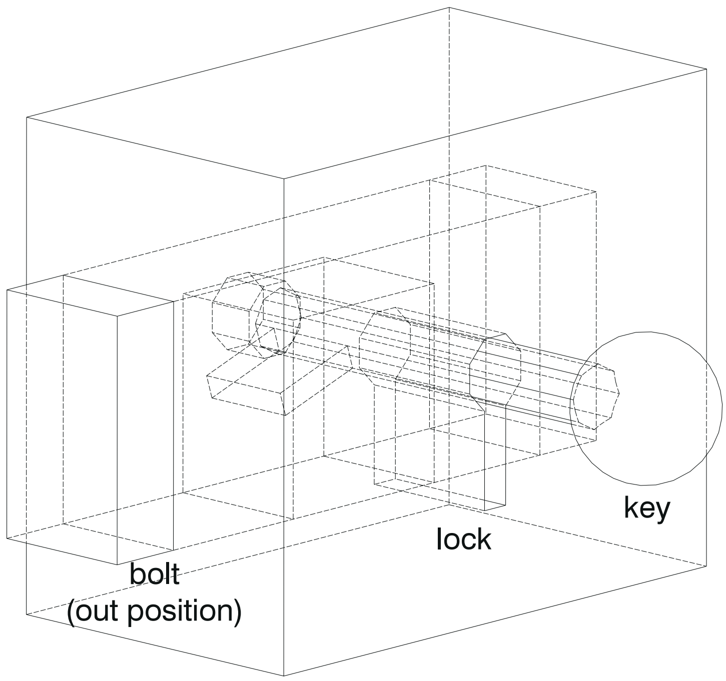

Figure 24: Sample 3-D Haptic Task: Key Inserted into Lock and Pushing Bolt

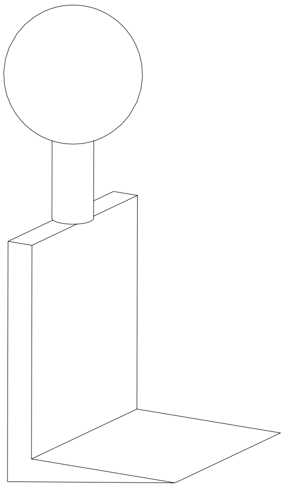

Figure 25: Tool Shape for Block Manipulation

The overall effectiveness or realism of the interaction may be a strongly subjective quality that is perceived differently by novice users, experienced users, and its programmer. The perceived reality of simulated objects is expected to depend heavily on whether the user is already familiar with the object and the interaction device and what expectations he or she has. Accordingly, it would be advantageous to ask test subjects to rate the effectiveness, realism, and ease of use of the haptic interface system rather than to rely on the biased impressions of the designer and programmer.

A small representative sample (5-10 people) of volunteer users will be introduced to the haptic interaction system and asked to perform a "blocks world" task and the key locking task both manually with the fabricated objects and in simulation with the haptic interface. The times, methods, and motions used to complete the tasks will be recorded and compared as well as the subjective ratings and impressions of the realism of the interaction. The purpose of the user evaluation is to approximately judge and verify the perceived effectiveness of the haptic interaction system; more statistically valid survey results would require carefully controlled conditions and a much larger sample size.

13 Proposed Contributions

Since haptic interface development is an emerging field of research, there is an opportunity to make a significant contribution by demonstrating a novel and fully operational system for 3-D haptic interaction. The main original contributions of this work will be in the integration of the technologies of realtime physical simulation and Lorentz magnetic levitation. Benefits from the proposed research are listed as follows:

Integration The methods used to separate the simulation and the device control computations and to maintain correspondence between the two systems will be applicable to other 6-DOF rigid-body device control interfaces. The intermediate representation developed to link the simulation at 30 Hz and the device controller at 1000 Hz will be a new extension of intermediate representations developed for point-based haptic interaction. Derivation of the spatial impedance control parameters from the intermediate representation will also be a new contribution.

Surface Effects The incorporation of friction and texture for rigid-body haptic tool interaction techniques with a physically-based modelling system will be a new contribution for realistic interaction.

Evaluation Thorough evaluations of the effectiveness and usability of the complete haptic interface system described will be a benchmark for comparison with future systems. The simulated tasks and environments set up for evaluation of haptic interaction are generalizable to a wide range of specific tasks involving haptic sensing.

Applications The documentation of the complete system design will enable more maglev haptic interfaces to be easily fabricated for CAD, medical, human factors applications. The interaction methods used will be applicable to rigid-body tool teleoperation systems as well as simulations.

Most of the integration methods and haptic rendering techniques developed will not be specific to maglev actuation, but will be applicable to any other type of high-performance haptic interface device.

Research Plan

Design	Winter 1996–Fall 1996
Fabrication	Spring 1996–Winter 1997
Control	Winter 1997–Summer 1997
Proposal	Spring 1997–Summer 1997
Build Aluminum Flotor	Summer 1997
Performance Testing	Spring 1997–Fall 1997
Integration with Simulation	Fall 1997–Winter 1998
Friction and Texture	Fall 1997–Spring 1998
Demonstration of System	Winter 1998–Spring 1998
Interaction Evaluation	Spring 1998–Summer 1998
Thesis Document	Summer 1998–Fall 1998

Acknowledgements

Many of the ideas and methods proposed emerged from discussions with Ralph Hollis and David Baraff. Several other lab members have worked on aspects of the maglev device development at one time or another. Zack Butler performed early characterization of the large position sensing photodiodes and designed the sensor circuitry and assemblies. Stella Yu formulated the iterative kinematics solution method used. Our 1996 summer student Chris Donohue worked on selection, acquisition and assembly of the system enclosure, VMEbus, and power supplies.

References

[1] K. Shimoga, "A survey of perceptual feedback issues in dexterous telemanipulation: Part i. finger force feedback," in *Proceedings of the IEEE Virtual Reality Annual International Symposium*, (New York), pp. 263–270, January 1993.

[2] R. Cholewiak and A. Collins, "Sensory and physiological bases of touch," in *The Psychology of Touch* (M. A. Heller and W. Schiff, eds.), Hillsdale, NJ: Lawrence Erlbaum Associates, 1991.

[3] R. L. Hollis and S. E. Salcudean, "Lorentz levitation technology: a new approach to fine motion robotics, teleoperation, haptic interfaces, and vibration isolation," in *Proc. 6th Int'l Symposium on Robotics Research*, (Hidden Valley, PA), October 2-5 1993.

[4] G. Burdea, *Force and Touch Feedback for Virtual Reality.* New York: Wiley and Sons, Inc., 1996.

[5] N. Durlach and A. Mavos, eds., *Virtual Reality: Scientific and Technological Challenges*, ch. 4. National Academy Press, 1995.

[6] D. A. Lawrence and J. D. Chapel, "Performance trade-offs for hand controller design," in *IEEE Int'l Conf. on Robotics and Automation*, (San Diego), pp. 3211–3216, May 1994.

[7] J. E. Colgate and J. M. Brown, "Factors affecting the Z-range of a haptic display," in *IEEE Int'l Conf. on Robotics and Automation*, (San Diego), pp. 3205–3210, May 1994.

[8] F. Brooks, Jr., M. Ouh-Young, J. J. Batter, and P. Kilpatrick, "Project GROPE—haptic displays for scientific visualization," *Computer Graphics*, vol. 24(4), pp. 177–185, August, 1990.

[9] K. Waters and S. Wang, "A 3D interactive physically-based micro world," in *Proc. SPIE (Extracting meaning from complex data: processing, display, interaction)*, vol. 1259, (Santa Clara, CA), pp. 91–98, Feb. 14-16 1990.

[10] Space Control GmbH/Logitech, Germany, *Magellan/Space Mouse User's Manual*, version 5.3 ed.

[11] M. Bergamasco, B. Allota, L. Bosio, L. Ferretti, G. Parrini, G. M. Prisco, F. Salsedo, and G. Sartini, "An arm exoskeleton system for teleoperation and virtual environments applications," in *IEEE Int'l Conf. on Robotics and Automation*, (San Diego), pp. 1449–1452, May 1994.

[12] S. Jacobsen, F. Smith, D. Backman, and E. Iversen, "High performance, high dexterity, force reflective teleoperator II," in *ANS Topical Meeting on Robotics and Remote Systems*, (New York), February 1991.

[13] B. Marcos, "Sensing, perception, and feedback for VR," in *VR Systems Fall 93 Conference*, (New York), SIG Advanced Applications, 1993.

[14] M. L. Agronin, "The design of a nine-string six-degree-of-freedom force-feedback joystick for telemanipulation," in *Proc. NASA Workshop on Space Telerobotics*, pp. 341–348, 1987.

[15] R. Lindemann and D. Tesar, "Construction and demonstration of a 9-string 6 dof force reflecting joystick for telerobotics," in *Proceedings of NASA International Conference on Space Telerobotics*, (NASA, Greenbelt, MD), pp. 55–63, Vol. 4 1989.

[16] M. Sato, Y. Hirata, and H. Kawarada, "Space interface device for artificial reality—SPIDAR," *Syst. Comput. Jpn. (USA)*, vol. 23, no. 12, pp. 44–54, 1992.

[17] T. Massie and K. Salisbury, "The PHANToM haptic interface: A device for probing virtual objects," in *Proceedings of the ASME Winter Annual Meeting, Symposium on Haptic Interfaces for Virtual Environment and Teleoperator Systems*, (Chicago, Illinois), November 1994.

[18] V. Hayward, J. Choksi, G. Lanvin, and C. Ramstein, "Design and multi-objective optimization of a linkage for a haptic interface," in *ARK'94, 4th Int'l Workshop on Advances in Robot Kinematics*, (Ljubliana, Slovenia), June 1994.

[19] H. Iwata, "Artificial reality with force-feedback: development of desktop virtual space with compact master manipulator," *Computer Graphics*, vol. 24(4), pp. 165–170, 1990.

[20] V. Hayward, "Toward a seven axis haptic device," in *Int'l Conf. on Intelligent Robots and Systems*, (Pittsburgh), pp. 113–139, August 1995.

[21] J. W. Hill, P. S. Green, J. F. Jensen, Y. Gorfu, and A. S. Shah, "Telepresence surgery demonstration system," in *IEEE Int'l Conf. on Robotics and Automation*, (San Diego), pp. 2302–2307, May 1994.

[22] I. Hunter, T. Doukoglou, S. Lafontaine, P. Charette, L. Jones, M. Sagar, and P. Hunter, "A teleoperated microsurgical robot and associated virtual environment for eye surgery," *Presence*, vol. 2, no. 4, pp. 265–280, 1994.

[23] S. Singh, M. Bostrom, D. Popa, and C. Wiley, "Design of an interactive lumbar puncture simulator with tactile feedback," in *IEEE Int'l Conf. on Robotics and Automation*, (San Diego), pp. 1734–1739, May 1994.

[24] R. L. Hollis, S. Salcudean, and A. P. Allan, "A six degree-of-freedom magnetically levitated variable compliance fine motion wrist: design, modeling, and control," *IEEE Transactions on Robotics and Automation*, vol. 7, pp. 320–332, June 1991.

[25] S. Salcudean, N.M. Wong, and R.L. Hollis, "Design and control of a force-reflecting teleoperation system with magnetically levitated master and wrist," *IEEE Transactions on Robotics and Automation*, vol. 11, pp. 844–858, December 1995.

[26] P. J. Berkelman, R. L. Hollis, and S. E. Salcudean, "Interacting with virtual environments using a magnetic levitation haptic interface," in *Int'l Conf. on Intelligent Robots and Systems*, (Pittsburgh), August 1995.

[27] S. Salcudean and T. Vlaar, "On the emulation of stiff walls and static friction with a magnetically levitated input-output device," in *International Mechanical Engineering Congress and Exposition*, (Chicago), pp. 303–309, November 1994.

[28] P. J. Berkelman, Z. J. Butler, and R. L. Hollis, "Design of a hemispherical magnetic levitation haptic interface device," in *Proceedings of the ASME Winter Annual Meeting, Symposium on Haptic Interfaces for Virtual Environment and Teleoperator Systems*, (Atlanta), November 17-22 1996.

[29] T. Yoshikawa, "Manipulability of robotic mechanisms," *International Journal of Robotics Research*, vol. 4, no. 2, pp. 3–9, 1985.

[30] E. Fasse, "On the spatial compliance of parallel manipulators and levitated platforms," in *ASME IMECE*, (San Diego), April 1997.

[31] E. D. Fasse and N. Hogan, "Quantitative measurement of haptic perception," in *IEEE Int'l Conf. on Robotics and Automation*, (San Diego), pp. 3199–3204, May 1994.

[32] M. Srinivasan, G. Beauregard, and D. Brock, "The impact of visual information on the haptic perception of stiffness in virtual environments," in *Proceedings of the ASME Winter Annual Meeting, Symposium on Haptic Interfaces for Virtual Environment and Teleoperator Systems*, (Atlanta), November 17-22 1996.

[33] N. Parker, S. Salcudean, and P. Lawrence, "Application of force feedback to heavy duty hydraulic machines," in *IEEE Int'l Conf. on Robotics and Automation*, (Atlanta), pp. 375–381, May 1993.

[34] D. Baraff and A. Witkin, "Dynamic simulation of non-penetrating flexible bodies," in *Computer Graphics* (*Proc. SIGGRAPH*), vol. 26, pp. 303–308, ACM, July 1992.

[35] D. Baraff, "Issues in computing contact forces for non-penetrating rigid bodies," *Algorithmica*, vol. 10, pp. 292–352, 1993.

[36] D. Baraff, "Coping with friction for non-penetrating rigid body simulation," in *Computer Graphics* (*Proc. SIGGRAPH*), vol. 25, pp. 31–40, ACM, July 1991.

[37] M. Minsky, M. Ouh-young, O. Steele, F. P. Brooks, Jr., and M. Behensky, "Feeling and seeing: issues in force display," *Computer Graphics*, vol. 24(2), pp. 235–243, 1990.

[38] M. Bailey, D. Johnson, T. Massie, R. Taylor, and M. Yim, "Haptic explorations with the Phantom: Virtual touch through point interaction," in *So Real I Can Almost Touch It: The Use of Touch as an I/O Device for Graphics and Visualization*, New Orleans, Louisiana: Siggraph Course Notes 37, 1996.

[39] J. Colgate, M. Stanley, and J. Brown, "Issues in the haptic display of tool use," in *Int'l Conf. on Intelligent Robots and Systems*, (Pittsburgh), August 1995.

[40] C. Zilles and J. Salisbury, "A constraint-based god-object method for haptic display," in *Int'l Conf. on Intelligent Robots and Systems*, (Pittsburgh), August 1995.

[41] K. Siira and D. Pai, "Haptic texturing: A stochastic approach," in *IEEE Int'l Conf. on Robotics and Automation*, (Minneapolis), pp. 557–562, April 1996.

[42] W. Mark, S. Randolph, M. Finch, J. V. Werth, and R. Taylor, "Adding force feedback to graphics systems," in *Computer Graphics (Proc. SIGGRAPH)*, pp. 447–452, 1996.

[43] Y. Adachi, T. Kumano, and K. Ogino, "Intermediate representation for stiff virtual objects," in *Proc. IEEE Virtual Reality Annual Intl. Symposium*, (Research Triangle Park, N. Carolina), pp. 203–210, March 1995.

[44] S. Vedula and D. Baraff, "Force feedback in interactive dynamic simulation," in *Proceedings of the First PHANToM User's Group Workshop*, (Dedham, MA), September 1996.